Excitonic absorption in asymmetric double quantum wells in an intense terahertz field: Coulombic coupling and Stark effects

J.-Z. Zhang* and D. Allsopp
Department of Electronic and Electrical Engineering, University of Bath, Bath BA2 7AY, United Kingdom
(Received 13 June 2009; revised manuscript received 10 November 2009; published 21 December 2009)

Optical absorption is calculated for asymmetric double quantum wells in intense terahertz (THz) fields applied parallel to the growth direction z. Owing to the lack of inversion symmetry, strong Coulombic coupling (CC) occurs between excitons. The effects of CC and various Stark effects due to the THz field-exciton interactions on the excitonic absorption are systematically studied. The absorption spectra show a rich variety of behaviors, including excitonic sidebands and replicas as well as peak splittings. Due to the optical Stark effect (OSE), Autler-Townes (AT) splittings occur in resonant THz fields whose frequency is near the transition frequency connecting two exciton energy levels, with the absorption of each exciton splitting into a double peak. Taking CC into account causes a pronounced asymmetry in the AT doublets as the oscillator strength is transferred from the higher-energy exciton to the lower of the pair. In a low-frequency driving THz field, multiple features emerge in the vicinity of the strong exciton peak, being separated from it by multiples of the THz-photon energy, $n\hbar\Omega$ ($n=\pm1,\pm2,\pm3,\ldots$). The multiple features are the THz-photon sidebands and replicas of the exciton and arise from different band-to-band transitions. The occurrence of the sidebands and replicas is proved to be due to the second-order Stark effect (SOSE). Including CC, the excitonic absorption connected with weak band-to-band transitions can occur with a great strength, and the overall absorption is significantly enhanced for a wide range of THz frequencies. The features of the AT splittings, the excitonic sidebands and replicas, and their variation with the THz field are well explained in terms of the CC and the Stark effects (OSE and SOSE).

DOI: 10.1103/PhysRevB.80.245320 PACS number(s): 71.35.Cc, 71.70.Ej, 78.20.Jq, 78.67.De

I. INTRODUCTION

The interband optical properties of quantum wells (QWs) are affected by electric fields. A dc electric field applied along the QW growth direction modulates the interband absorption by the quantum-confined Stark effect (QCSE). Since the experimental observation of the QCSE (Ref. 1) the electro-optical absorption for dc biased QWs has been the subject of intense research. An ac electric field applied normal to QWs also modulates the interband absorption, and in particular the electro-optic (EO) modulation by a terahertz (THz) electric field is of great interest. The THz EO modulation requires the intersubband transitions in the conduction band and/or valence band to fall in the THz range. Coupled double QWs (CDQWs) are suitable structures as the intersubband transitions in both conduction and valence bands can be tuned to the THz frequencies by band-structure engineering (e.g., by adjusting the CDQW geometry). Particularly interesting are asymmetric double QWs (ADQWs), which consist of two QWs of different widths coupled through a thin middle barrier. By using ADQWs, mixing of a weak near-infrared (NIR) beam and a strong THz beam allows the generation of THz-optical sidebands of all orders, and efficient first- and second-order processes have been observed in early experiment.[2] Such THz EO effects have potential applications in nonlinear spectroscopy[3] as well as in ultrafast all-optical switching. Indeed, by means of the THz EO modulation,[2] wavelength conversion in GaAs/AlGaAs ADQWs has been experimentally demonstrated[4–6] with a conversion efficiency of 0.2% achieved.[5] Asymmetric QWs are attractive structures also for generation of broadband THz emission[7–10] by femtosecond interband photoexcitation (or optical rectification[3]). From the viewpoint of basic research, the ADQW structure is also a quantum-mechanical model system for the study of optical coherence effects under the influence of an intense slowly varying field.

In an atom, an oscillating electric field couples two atomic levels via the dipole interaction, and when the field is intense it mixes with the two atomic states forming renormalized states (the atom is then called a dressed atom[11]). In general, the energy spectrum of the renormalized states is quite complicated and is dependent on the field frequency and the dipole interaction strength. However, two limiting cases are of great interest in which approximate analytical solutions exist for the renormalized states yielding the Stark effects.[12] The first is the resonant field case: when the field frequency is near to the transition frequency that connects the two energy levels, each level splits into two sublevels corresponding to a pair of renormalized states, with an energy separation given by the Rabi energy.[11] Each pair of such renormalized states contain similar components from their common unperturbed atomic state. This is the optical Stark effect (OSE). The splitting of an atomic level in strong resonant fields yields splitting in absorption lines connected to the level, namely, the Autler-Townes (AT) splitting.[12] The second case is for low-frequency fields, in which the first-order Stark effect (FOSE) or the second-order Stark effect (SOSE) may occur, depending on the field intensity, when the line broadening is small. In the FOSE each atomic level breaks up into a number of components spaced by *one*-photon energy, with intensities depending on the field strength. For the SOSE each energy level breaks up into components with intervals of *two*-photon energy, with the principal component being shifted from the unperturbed atomic level. This energy shift and the intensi-

ties of all the components depend on the *square* of the field strength. The SOSE on absorption lines was first observed experimentally by Townes and Merritt.[13] For a semiconductor under weak photoexcitation, the interband absorption is determined by exciton absorption. When a strong THz field is applied additionally, it may couple exciton states, leading to optical Stark effects as in the atomic system. Then the interband absorption is determined by the renormalized exciton states (of dressed excitons) due to the THz field-exciton interaction. However, caution should be taken in studying the Stark effects in the excitonic absorption of QWs because QWs have very intricate exciton states (distinct from true atomic states), which dictate the THz field-exciton interaction. Due to quantum confinement in the growth direction, electron and hole subbands are formed. Conventionally a QW exciton can be associated with a certain pair of electron-hole (e-h) subbands[14,15] or the band-to-band transitions between the pair (for example, exciton X_{e1h1} is associated with electron subband $e1$ and hole subband $h1$ or the $h1$-$e1$ band-to-band transitions). As the THz field induces intersubband transitions by interacting with an electron or a hole, it interacts with excitons via the induced dipole moments. Thus, two such exciton states that may couple via the dipole interaction should be connected with one common electron or hole subband (for example, both exciton states of X_{e1h1} and X_{e1h2} are connected to electron subband $e1$). This is a general selection rule that governs the THz-field-induced transitions between exciton states, but further selection rules may apply when the electronic system has certain symmetry. More intricacies however arise owing to Coulombic coupling (CC) of QW exciton states. The CC occurs as quantum mechanically the electron (hole) in an e-h pair is scattered between *different* electron (hole) subbands due to the e-h Coulomb interaction. As a result, the exciton state of X_{e1h1}, for instance, whose main component is due to the e-h subband pair $(e1,h1)$, may also contain components from other subband pairs, e.g., from pair $(e1,h2)$, when there is CC between excitons X_{e1h1} and X_{e1h2}, which are associated with the two subband pairs.[16] Such CC between different excitons has a major influence on the interband absorption of coupled QWs.[17] The CC should not be confused with the Coulomb interaction within the same pair of e-h subbands. We need to clarify four points regarding the Coulombic coupling. First, in a symmetric QW, an electronic state is a symmetric or an antisymmetric state in the growth direction, with the consequence that there may be no CC between certain two excitons associated with two different subband pairs. In an asymmetric QW, in principle CC occurs between any exciton states due to symmetry breaking. Second, in symmetric QWs, while two exciton states are coupled by the dipole interaction arising from the THz electric field, no CC occurs between the two states. This can be proved from the expression for the Coulomb matrix elements (Sec. II below) by using the symmetry properties of the electronic states. In an asymmetric QW, two exciton states can be coupled by the CC and the dipole interaction simultaneously. We shall see below that these exciton states are indeed crucial to the evaluation of the interband absorption in THz-field-driven ADQWs. Third, the CC may be strong in ADQWs where electron or hole subbands are closely spaced. Fourth, without a THz field, CC occurs between excitons in ADQWs. In the presence of an intense THz field, CC then will occur between the dressed excitons; that is, there is mixing between the renormalized exciton states due to the Coulomb interaction.

There have been theoretical studies of the optical absorption in QWs under intense THz irradiation. In the studies of the dynamical Franz-Keldysh effect (DFKE) of the exciton absorption,[18,19] the THz wave oscillates in the QW layer plane, inducing transitions between the two-dimensional (2D) exciton states. To induce intersubband transitions, the THz field needs to be applied along the QW growth direction. Early absorption studies in such THz-field-driven QWs were focused on single QWs. Liu and Ning[20] calculated interband absorption for a symmetric QW populated by carriers and considered the case that a strong far-infrared field couples with the intersubband transitions between two conduction subbands only. Maslov and Citrin[21] calculated linear optical absorption for an infinitely deep QW, where only the valence subbands are coupled by the applied THz field. Both studies found Autler-Townes splittings in the excitonic absorption lines when two conduction[20] or valence[21] subbands are coupled by a near-resonant field. These excitonic AT splittings show similar behavior to the AT splitting in atoms, as there is no Coulombic coupling between the exciton states involved.[20,21] In a further study,[22] Maslov and Citrin calculated interband absorption for a THz field with *low* frequency compared with the subband energy spacing. Specifically they investigated what happens when the low-frequency field couples the exciton states of X_{e1h1} and X_{e1h2}. They found that two replicas appear about the absorption of each exciton. The two replicas around the X_{e1h1} peak are separated from X_{e1h1} by two THz-photon energy, whereas the two replicas about exciton X_{e1h2} are located one THz-photon energy from X_{e1h2} while the X_{e1h2} peak itself is absent. Interestingly, when a strong dc bias is applied in addition to the THz field, multiple replicas emerge on both sides of each excitonic absorption peak: the replicas around the exciton peak are separated from it by an integer number of the THz-photon energy. However, the mechanisms behind the occurrence of the replicas are unclear and the bias dependence of the exciton peaks and replicas remains unresolved.

The interband absorption in THz-field-driven ADQWs can be measured using pump-probe reflection or transmission experiments. In this paper we model such a setup based on a cw-THz pump beam and a tunable cw-NIR probe beam being used. The absorption of the probe beam in the presence of the pump is then explored as a function of the NIR photon energy, the frequency, and the intensity of the THz field. This study is based on a numerical calculation of the ADQW interband polarization, taking into account the conduction subbands that may couple by the THz field as well as the valence subbands. Particular attention is paid to the excitonic levels that are coupled simultaneously by the Coulombic interaction and the THz field. We study the THz-field dependence of the interband excitonic absorption in terms of the spectral shift, splitting, and intensity variation. The main issue we address is how the CC and Stark effects affect the excitonic absorption. For this purpose, we compare the absorption spectra calculated with and without CC, focusing on how the spectra vary with the intensity and frequency of the

THz field. We found that, when the CC is excluded, the shifts and splittings in the absorption spectra comply with the Stark effects as in the atomic system. On the other hand, including CC can change significantly the absorption spectra in both the near-resonant and low-frequency THz-field cases. We also investigate how the various replicas occur around the absorption positions of excitons in low-frequency THz fields, producing a comprehensive study of THz induced effects in QWs to explain fully observed behavior.

This paper is organized as follows. In Sec. II, a model for the calculation of the interband polarization and absorption, including excitonic effects, Coulombic coupling, and THz-field-induced coupling between exciton states in THz-field-driven QWs is presented. The derivation of the interband polarization equation is outlined, and an effective method of solving it is described, in terms of handling the Coulomb singularity, for the calculation of the absorption in accordance with the pump-probe setup mentioned above. In Sec. III, we present results of the interband absorption for a three-subband electronic system, which involves two exciton states associated with two different subband pairs. Particular attention is paid to the absorption when (i) a near-resonance and (ii) a low-frequency THz field are applied. This allows us to check our numerical results against the analytical expressions that can be sought, for the case where the CC is excluded, and then further explore what happens when the CC is taken into account. A detailed discussion is made to the case of low-frequency THz fields, regarding the excitonic sidebands and replicas obtained. Further we present absorption results obtained by including more subbands, for THz fields at a number of THz frequencies and intensities. The CC and Stark effects on the absorption and the spectral variation with the THz frequency are discussed in detail. Finally, Sec. IV summarizes the main results obtained. In the Appendix, using a three-level model (two excitonic levels plus the semiconductor ground state) for the electronic system that interacts with two light fields, a density-matrix derivation of the optical susceptibility is outlined, yielding the AT splitting for the near-resonant THz field and the SOSE and FOSE for the low-frequency THz field. Transparent expressions for the susceptibility are obtained and are used to interpret spectral features obtained from the numerical calculation.

II. MODEL

The QW structure which we consider is an asymmetric coupled quantum well, which consists of two quantum wells with different well widths. The electron and hole states are calculated using the effective-mass approximation. The single-particle Hamiltonian can be written as

$$H_0(\mathbf{r}) = -\frac{\hbar^2}{2m_{\|}^*}\left(\frac{\partial^2}{\partial^2 x}+\frac{\partial^2}{\partial^2 y}\right)-\frac{\hbar^2}{2}\frac{\partial}{\partial z}\frac{1}{m_{\perp}^*(z)}\frac{\partial}{\partial z}+V(z), \quad (1)$$

where $m_{\perp}^*(z)$ is used to distinguish the electron (or hole) effective mass for motion in the growth direction in the wells from that in the barriers, and $m_{\|}^*$ is the effective mass for motion in the QW layer plane. $V(z)$ is the ADQW potential, which is determined by the band offsets of the conduction (or valence) bands in the different well and barrier regions. To solve the eigenequation of H_0, the envelope function of the subband state is expanded in terms of the bulk plane waves. By imposing the periodic boundary condition, the eigenequation is then transformed into a set of secular equations, which are solved using standard numerical diagonalization technique. Thus, we obtain the electron envelope function $\Phi_{n\mathbf{k}}^e(\mathbf{r})=\frac{1}{\sqrt{A}}f_n(z)e^{i\mathbf{k}\cdot\boldsymbol{\rho}}$ and eigenenergy $E_{nk}^e=\varepsilon_n^e+\hbar^2k^2/(2m_{e\|}^*)$, where n is the electron subband index, $\mathbf{k}$ is the 2D wave vector in the QW layer plane, and $f_n(z)$ is the confinement envelope function in the z direction corresponding to energy ε_n^e. $\boldsymbol{\rho}=(x,y)$ is the 2D in-plane position vector, A is the sample area parallel to the QW plane, and $m_{e\|}^*$ the electron effective mass for motion in the QW layer plane. Similarly we find the hole envelope function $\Phi_{l\mathbf{k}}^h(\mathbf{r})=\frac{1}{\sqrt{A}}g_l(z)e^{i\mathbf{k}\cdot\boldsymbol{\rho}}$ and eigenenergy $E_{lk}^h=\varepsilon_l^h+\hbar^2k^2/(2m_{h\|}^*)$, where l indexes the hole subband and $m_{h\|}^*$ is the hole effective mass for motion in the layer plane. We use *en* and *hl* to denote the electron subband of index n and the hole subband of index l, respectively.

In second quantization the Hamiltonian for the QW system in the presence of an optical field and THz radiation simultaneously can be written as

$$\begin{aligned}H=&\sum_{\mathbf{k}}\left[\sum_n (E_{n\mathbf{k}}^e+E_g)a_{n\mathbf{k}}^\dagger a_{n\mathbf{k}}+\sum_l E_{l\mathbf{k}}^h b_{l-\mathbf{k}}^\dagger b_{l-\mathbf{k}}\right]\\&-\sum_{n',n,l',l}\sum_{\mathbf{k},\mathbf{k}',\mathbf{q}} a_{n'\mathbf{k}+\mathbf{q}}^\dagger b_{l\mathbf{k}'-\mathbf{q}}^\dagger b_{l'\mathbf{k}'}a_{n\mathbf{k}}V_{n'nl'l}(q)\\&-\sum_{n,l,\mathbf{k}}(\mu_{nl\mathbf{k}}a_{n\mathbf{k}}^\dagger b_{l-\mathbf{k}}^\dagger+\mu_{nl\mathbf{k}}^* b_{l-\mathbf{k}}a_{n\mathbf{k}})E_\omega\\&-\left(\sum_{n'n\mathbf{k}}\xi_{n'n}a_{n'\mathbf{k}}^\dagger a_{n\mathbf{k}}-\sum_{l'l\mathbf{k}}\zeta_{ll'}b_{l'-\mathbf{k}}^\dagger b_{l-\mathbf{k}}\right)E_\Omega, \quad (2)\end{aligned}$$

where $a_{n\mathbf{k}}^\dagger, a_{n\mathbf{k}}$ are the creation and annihilation operators for the electron in state $|n\mathbf{k}\rangle$ and $b_{l\mathbf{k}}^\dagger, b_{l\mathbf{k}}$ are the creation and annihilation operators for the hole in state $|l\mathbf{k}\rangle$. The first term of H is the free-carrier energy where E_g is the band gap of the well material, and the second term describes the e-h Coulomb interaction. The third term is the dipole interaction between the optical electric field $\mathbf{E}_\omega$ and the induced interband polarization, and the fourth term describes the interaction of the z-polarized THz field E_Ω ($E_\Omega=E_T\cos\Omega t$) with the induced intersubband transitions in the conduction and valence bands. Note that, for clearness, in Eq. (2) the index for spin has been absorbed into $\mathbf{k}$. $\mu_{nl\mathbf{k}}$ is the interband dipole matrix element for the transition between the electron state $|n\mathbf{k}\rangle$ and hole state $|l\mathbf{k}\rangle$, $\mu_{nl\mathbf{k}}=\mu_0\langle\Phi_{n\mathbf{k}}^e|\Phi_{l\mathbf{k}}^h\rangle$, where $\mu_0=\langle u_c|\bar{e}\mathbf{r}\cdot\boldsymbol{\varepsilon}|u_v\rangle$ is the optical dipole matrix element between the bulk Bloch states of the conduction and valence bands, $|u_c\rangle$ and $|u_v\rangle$. Here, $\bar{e}=-e$ is the free-electron charge and $\boldsymbol{\varepsilon}$ is the unit vector of the electric field $\mathbf{E}_\omega$, which lays in the QW plane for the transverse electric (TE) polarization or is in the growth direction z for the transverse magnetic polarization. $\xi_{n'n}=\langle f_{n'}|\bar{e}z|f_n\rangle$ ($\zeta_{ll'}=\langle g_l|\bar{e}z|g_{l'}\rangle$) is the intersubband dipole matrix element for the transitions between a pair of conduction subbands n,n' (valence subbands l,l'). The Coulomb matrix elements in Eq. (2) are given by[23,24]

$$V_{n'nl'l}(q) = \frac{2\pi e^2}{A\epsilon_b q}\mathcal{F}_{n'nl'l}(q), \tag{3}$$

where ϵ_b is the background dielectric constant, q is the modulus of the 2D transfer wave vector $\mathbf{q}$, and the form factor

$$\mathcal{F}_{n'nl'l}(q) = \int dz_e \int dz_h \, f^*_{n'}(z_e) f_n(z_e) e^{-q|z_e - z_h|} g^*_{l'}(z_h) g_l(z_h) \tag{4}$$

averages over the electron and hole distributions in the ADQW. The subband indices n and l denote the initial subbands occupied by the interacting electron and hole, respectively, and the indices n' and l' denote the final subbands after the e-h scattering. In a symmetric quantum well, any electron (hole) envelope function in the z direction has a definite even or odd parity. Therefore, there are possible nonzero Coulomb matrix elements $V_{n'nl'l}(q)$ only when (i) the confinement envelope functions of the initial and final electron subbands, $f_n(z_e)$ and $f_{n'}(z_e)$, are of the same parity, while for the hole subband states, the envelope functions $g_l(z_h)$ and $g_{l'}(z_h)$ have the same parity; or (ii) $f_n(z_e)$ and $f_{n'}(z_e)$ have different parities while $g_l(z_h)$ and $g_{l'}(z_h)$ have different parities. In an asymmetric quantum well however nonzero Coulomb matrix elements $V_{n'nl'l}(q)$ may exist for any two subband pairs, (n,l) and (n',l'), as neither the electron nor hole states have inversion symmetry.

Optical absorption occurs due to the macroscopic interband polarization $P(t)$ induced by the NIR probe in the THz-field-driven ADQW. Quantum mechanically $P(t)$ is connected to the microscopic interband coherence, which is defined as[25] $p_{ln\mathbf{k}} = b_{l-\mathbf{k}} a_{n\mathbf{k}}$. Using the Heisenberg equation, the equation of motion for $p_{ln\mathbf{k}}$ can be obtained from the Hamiltonian H as follows:

$$\begin{aligned}\frac{\partial p_{ln\mathbf{k}}}{\partial t} = &-\frac{i}{\hbar}(E^e_{n\mathbf{k}} + E^h_{l\mathbf{k}} + E_g)p_{ln\mathbf{k}} + \frac{i}{\hbar}\mu_{nl\mathbf{k}}E_\omega \\ &+ \frac{i}{\hbar}\sum_{l',n',\mathbf{k}'} V_{nn'l'l}(|\mathbf{k}-\mathbf{k}'|)p_{l'n'\mathbf{k}'} \\ &+ \frac{i}{\hbar}E_\Omega\left(\sum_{n'}\xi_{nn'}p_{ln'\mathbf{k}} - \sum_{l'}\zeta_{l'l}p_{l'n\mathbf{k}}\right) + \left.\frac{\partial p_{ln\mathbf{k}}}{\partial t}\right|_{col}.\end{aligned} \tag{5}$$

The terms containing the Hartree-Fock contributions[25] are written explicitly, while the corrections from higher-order correlations (collision terms) are incorporated into $(\partial p_{ln\mathbf{k}}/\partial t)|_{col}$. In the dephasing time approximation,[25] $(\partial p_{ln\mathbf{k}}/\partial t)|_{col} = -\gamma_p p_{ln\mathbf{k}}$, where γ_p is the polarization dephasing rate from carrier-phonon scattering. The polarization components $p_{ln\mathbf{k}}$ are associated with an e-h pair created by optical excitation. If the electron is in subband en and the hole in subband hl, then the pair will be bound by the attractive e-h Coulomb interaction, forming an exciton that is referred to as the hl-en exciton, X_{enhl}. In this exciton the binding of the e-h pair results from the coupling of the polarization components, $p_{ln\mathbf{k}}$ and $p_{ln\mathbf{k}'}$, at different wave vectors but with the same electron and hole subbands, via the Coulomb matrix elements $V_{nnll}(|\mathbf{k}-\mathbf{k}'|)$. What happens in actual QWs is not so simple, as the electron (hole) can also be in different subbands from en (hl), forming excitons such as $X_{en'hl}$. Then excitons $X_{en'hl}$ and X_{enhl} will couple if nonzero Coulomb matrix elements $V_{nn'll}(q)$ and $V_{n'nll}(q)$ exist. It is the coupling of the polarization components $p_{ln\mathbf{k}}$ and $p_{ln'\mathbf{k}'}$ via these Coulomb matrix elements that causes the Coulombic coupling between the two excitons. In fact in ADQWs there is really no such thing as a pure exciton state of X_{enhl} or $X_{en'hl}$ but a mixed $(X_{enhl}, X_{en'hl})$ state due to the excitonic mixing. The CC occurs between the two excitons and, when the THz field is strong, it occurs between the dressed excitons. Equation (5) also indicates that different interband polarization components at the same wave vector, for example, $p_{ln\mathbf{k}}$ and $p_{ln'\mathbf{k}}$ couple due to the dipole interaction of the THz field with the induced intersubband polarization. Therefore, the interband polarization induced by the NIR probe field is affected by the excitonic mixing (the third term) and modulated by the THz field (the fourth term). THz-optical mixing occurs in the ADQW as the THz field causes the various frequency components of the optical polarization to couple. We note that for weak NIR fields the dynamics of the intersubband polarization and the carrier population have been neglected.

To find solutions $p_{ln\mathbf{k}}(t)$ the coupled polarization equations [Eq. (5)] are numerically solved in wave-vector space and time domain using a fourth-order Runge-Kutta method. We assume that $p_{ln\mathbf{k}}$ depends on the magnitude of the 2D $\mathbf{k}$ only, as the interband polarization here is mainly contributed from the s states of the QW excitons. In the time domain, the continuous-wave NIR field in experiments[2,4–6] is approached by using an optical pulse $E_\omega(t) = E_0(\cos\omega t)e^{-t^2/\tau^2}$ with a very narrow spectrum (spectral width of <0.4 meV), where the duration τ relates to the full width at half maximum (FWHM) in irradiance, $\sqrt{2\ln 2}\,\tau$, of the pulse. The rotating-wave approximation[26] is used such that the fast-varying part of the time-dependent polarization components $p_{ln\mathbf{k}}(t)$ is approached by $e^{-i\omega t}$. Accurate evaluation of the Coulomb term in the polarization equation [Eq. (5)] is important in obtaining the correct solutions of $p_{ln\mathbf{k}}(t)$ and then the macroscopic polarization. On the other hand, the calculation should be efficient especially when the time domain is large (such as in long-duration pulses for the probe) and/or several electron and hole subbands are involved. Therefore, the singularity of the Coulomb potential needs to be properly treated. Here, we adopt the modified quadrature technique proposed by Chuang *et al.*[23] First we need to separate the Coulomb term into two parts: one part containing singularity and the other not. To do this, we replace $\Sigma_{\mathbf{k}'}$ by $\int k'dk'd\varphi$ and make a transformation to the Coulomb matrix elements [Eqs. (3) and (4)], such that the singularity in the Coulomb term is transferred into the integral,

$$v(k,k') = \frac{e^2}{2\pi\epsilon_b}\int_0^{2\pi}\frac{d\varphi}{[k^2 + (k')^2 - 2kk'\cos\varphi]^{1/2}}, \tag{6}$$

where φ is the angle between the two wave vectors $\mathbf{k}$ and $\mathbf{k}'$. The contribution of $v(k,k')$ to the Coulomb term in Eq. (5) is

given by the integral $Q_k=\int_0^\infty v(k,k')p_{lnk'}k'dk'$. The rest of the Coulomb term is due to the overlap integral[23] of the confinement envelope functions and a function of $|z_e-z_h|$,

$$F_q(|z_e-z_h|)=\frac{e^2}{2\pi\epsilon_b}\int_0^{2\pi}\frac{1}{q}(e^{-q|z_e-z_h|}-1)d\varphi. \quad (7)$$

The function $F_q(|z_e-z_h|)$ contains no singularity because its integrand is finite in the limit of $q=|\mathbf{k}-\mathbf{k}'|\to 0$. To handle the part with singularity, we rewrite the integral of Q_k as

$$\int_0^\infty v(k,k')p_{lnk'}k'dk'=\int_0^\infty v(k,k')[p_{lnk'}-\Lambda(k,k')p_{lnk}]k'dk' + p_{lnk}\int_0^\infty v(k,k')\Lambda(k,k')k'dk'. \quad (8)$$

The function $\Lambda(k,k')$ is chosen such that $\lim_{k'\to k}[p_{lnk'}-\Lambda(k,k')p_{lnk}]=0$, which cancels out the logarithmic singularity of $v(k,k')$, while the last term in Eq. (8) can be integrated analytically. In our calculation we choose $\Lambda(k,k')=2k^2/[k^2+(k')^2]$.[23] Introducing the normalized wave vector $\tilde{k}=ka_B$ [where $a_B=\hbar^2\epsilon_b/(e^2m_r^*)$ is the exciton Bohr radius and m_r^* is the reduced e-h mass, $1/m_r^*=1/m_e^*+1/m_h^*$], and letting $\tilde{k}=\tan(\pi x/2)$, the numerical integration over the wave vector is then transformed to the x space, which we calculate by using the Gauss-Legendre quadrature method. Here, $0\le x\le x_{cut}$, where the cutoff x_{cut} (the cutoff k_{cut} accordingly) is set to restrict the discrete k points to the Brillouin zone. In the actual calculation however smaller cutoff values can be used to save computing time.

Having obtained $p_{ln\mathbf{k}}(t)$, the interband polarization $P(t)$ is then calculated from $p(t)=\frac{1}{V}\Sigma_{n,l,\mathbf{k}}p_{ln\mathbf{k}}\mu_{nl\mathbf{k}}^*+\text{c.c.}$, where V is the volume of the QW. Fourier transformation of $P(t)$ gives the spectrum of the interband polarization $P(\omega)$ and the optical susceptibility $\chi(\omega)$ is then obtained, $\chi(\omega)=P(\omega)/E(\omega)$. The optical absorption coefficient relates to the susceptibility $\chi(\omega)$ (Ref. 25) via $\alpha(\omega)=4\pi\omega\ \text{Im}\ \chi^{(1)}/(cn_b)$, where n_b is the background refractive index and c is the speed of light in vacuum.

The investigated ADQW structure consists of undoped 75 and 85 Å GaAs wells separated by a 23 Å $Al_{0.3}Ga_{0.7}As$ middle barrier while embedded in two outer $Al_{0.3}Ga_{0.7}As$ barriers and corresponds to the practical structure used in the measurements reported in Ref. 2. Only the heavy-hole subbands are considered, as in the THz-optical mixing experiments[2,4–6,27,28] the NIR field is TE-polarized allowing the light-hole contribution to the interband polarization to be neglected. The material parameters for the band-structure calculation are taken from Ref. 29, and the alloy composition-dependent parameters are used where their bowing parameters are available. The parameters used for GaAs at low temperatures are $m_{e\|}^*=m_{e\perp}^*=0.067m_0$, $m_{h\|}^*=0.112m_0$, $m_{h\perp}^*=0.377m_0$ (m_0 is the free-electron mass), and $E_g=1.519$ eV; the parameters for $Al_{0.3}Ga_{0.7}As$ are $m_{e\perp}^*=0.092m_0$, $m_{h\perp}^*=0.401m_0$, and $E_g=1.937$ eV. The conduction- and valence-band offsets for $GaAs/Al_{0.3}Ga_{0.7}As$ are 253 and 165 meV, respectively. For the TE polarization, assuming $\boldsymbol{\varepsilon}\|\mathbf{x}$ the optical matrix element μ_0 is then

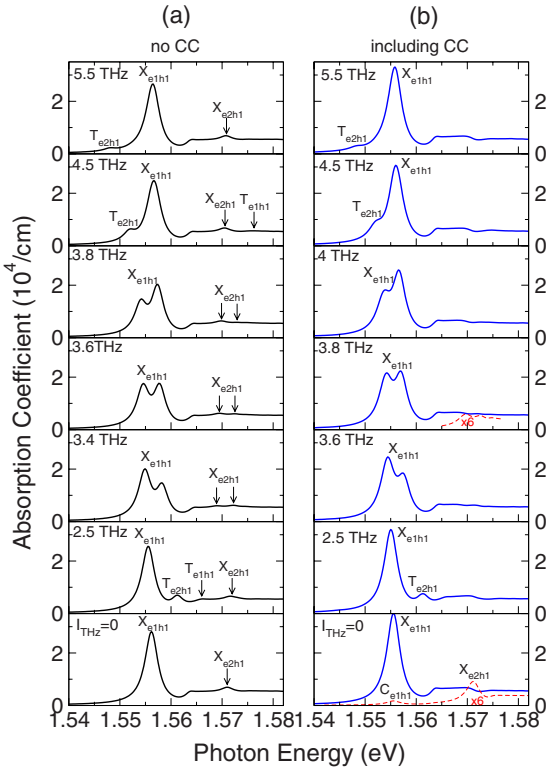

FIG. 1. (Color online) Interband absorption coefficients vs near-infrared (NIR) photon energy from $f=2.5$ to 5.5 THz at a THz field intensity of 0.5 MW/cm^2 in the GaAs/AlGaAs ADQW with Coulombic coupling (CC) excluded (left column) and included (right column). The bottom two graphs show interband absorption with no THz field (left: without CC; right: including CC). Three subbands are used in the calculation: the first and second electron subbands and the first hole subband.

$\mu_0=\langle u_c|\bar{e}x|u_v\rangle=e\hbar\sqrt{(E_p/4m_0)}/E_g$ (Ref. 30); for GaAs the energy parameter E_p is 28.8 eV (Ref. 29) thus yielding $\mu_0=4.87\ e$Å. The background dielectric constant is $\epsilon_b=12.4$. The dephasing rate we used is $\gamma_p=1.52$ THz, corresponding to the energy broadening of 2 meV.[2] In solving Eq. (5) and numerical integration, $k_{cut}=15(1/a_B)$ (this k_{cut} is about 10% the Brillouin-zone dimension), 150 quadrature points are used and good convergence is obtained. For the time domain, the FWHM in irradiance of the NIR pulse is 8 ps, and the number of time points used is 40 000.

III. RESULTS AND DISCUSSIONS

As mentioned in the above section, the interband absorption coefficient is proportional to the imaginary part of the first-order susceptibility. We start with a simpler case which involves two electron subbands $e1,e2$ and only one hole subband $h1$. We further ignore the Coulombic coupling between the X_{e1h1} and X_{e2h1} excitons, by setting the Coulomb matrix elements $V_{1211}(q)=V_{2111}(q)=0$. Figure 1(a) (*left-hand* column of graphs) shows the calculated absorption coefficient in the ADQW driven by a THz field of intensity $I_T=0.5$ MW/cm^2 with frequencies from 2.5 to 5.5 THz as indicated. For comparison, the absorption coefficient for the

ADQW with no THz field is also shown (bottom panel). The intensity of the THz wave refers to the intensity of the incident THz radiation in the air.[2] The THz field however entering the polarization equation [Eq. (5)] should be the field which is transmitted into the quantum well medium. For example, $I_T=0.5$ MW/cm^2 corresponds to the transmitted field strength of 8.5 kV/cm in the QW.[31] Without THz field the absorption spectrum features the two exciton peaks, X_{e1h1} and X_{e2h1}, and the continuum. The absorption of exciton X_{e2h1} is weak because of its small oscillator strength. The clear exciton peaks are present as the motions of the two excitons are separated in the decoupling approximation. There is no mixing between the exciton wave functions, which can be simplified and written as $\psi=\phi_\alpha(\boldsymbol{\rho})f_n(z_e)g_l(z_h)$, where α indexes for the ideal 2D exciton states[25] (α is the s states here) and $n=1$ (2) and $l=1$ are the electron and hole subband indices for exciton X_{e1h1} (X_{e2h1}). When the THz field is turned on, at a THz frequency of $f=2.5$ THz the X_{e1h1} peak shifts to the red while the X_{e2h1} absorption shifts to the blue. Two other features of absorption emerge. One feature, at the photon energy 1.5614 eV, is located at exactly one THz-photon energy ($\hbar\Omega=10.34$ meV) below the X_{e2h1} peak. It results from the $h1$-$e1$ transitions but is very weak compared to the exciton X_{e1h1} peak. This feature appears at such an energy position because an X_{e2h1} exciton can be created by simultaneous absorption of one NIR photon and one THz photon. Thus, it is referred to as a single THz-photon replica of X_{e2h1} and denoted as T_{e2h1}. Similarly, the other feature at the photon energy 1.5660 eV, which is located one THz-photon energy above the X_{e1h1} peak, is a single THz-photon replica of X_{e1h1} and denoted as T_{e1h1}. In previous DFKE calculations,[18,19] the THz field oscillating in the QW plane induces transitions between 2D exciton states $1s$ and $2p$; the single THz-photon replica of the $2p$ exciton was demonstrated, whose occurrence is similar to that of X_{e2h1}'s replica shown here. As the THz frequency increases the single photon replicas, T_{e2h1} and T_{e1h1}, shift toward the excitonic peaks X_{e1h1} and X_{e2h1}, respectively, and strengthen while the magnitude of the excitonic peaks decreases. When the THz field is near resonance with the two excitons, i.e., the THz frequency is close to the transition frequency connecting to the two excitonic levels, 3.6 THz, each sideband obtains similar strength to its main peak. In other words, each exciton peak of X_{e1h1} and X_{e2h1} at zero THz field now splits into two smaller doublets, and therefore there are four peaks. This is the Autler-Townes splitting,[12] the manifestation of the OSE in the linear absorption spectrum. As given in Appendix, Sec. 1, the energy splitting value is simply $\Delta=[\delta^2+4(\gamma^2+\Omega_R^2)]^{1/2}$, where δ is the detuning of the THz field from the resonance frequency. Ω_R is the Rabi frequency for the THz wave and characterizes the THz field-exciton interaction, $\Omega_R=\frac{1}{2}|\xi|E_T/\hbar$ (ξ the dipole matrix element connecting the two exciton states). Thus, we see from Fig. 1(a) that, in the on-resonance spectrum ($f=3.6$ THz) the absorption doublets of each exciton are approximately symmetric and equally strong. As f exceeds the resonant frequency of 3.6 THz, the excitonic splitting increases with the absorption doublets becoming asymmetric again. Now, as the THz frequency further increases the weaker doublet of X_{e1h1} continues to redshift, while the weaker doublet of X_{e2h1} continues to blueshift, with both strengths becoming weaker and weaker [see the two panels for 4.5 and 5.5 THz in Fig. 1(a)]. At sufficiently high THz frequencies the exciton states are unperturbed by the THz field, and a simple two exciton peak (X_{e1h1} and X_{e2h1}) absorption spectrum is restored. For example, the spectrum at $f=9.5$ THz (not shown) is more or less the same as that without THz field. The spectral AT splitting is due to the energy-level splitting of the OSE. Equations (A12) and (A15) of the density-matrix derivation show that, of the two exciton levels coupled by the THz field, each splits into two sublevels to give a total of four levels. From the calculated AT splitting values [Fig. 1(a)] we estimate the absolute value of the dipole matrix element ξ associated with the X_{e1h1} and X_{e2h1} exciton states to be 33.2 eÅ. In single QWs (Ref. 21) only one double absorption peak was found (see Figs. 2 and 3 in Ref. 21 where the THz field resonantly couples with X_{e1h1} and X_{e1h2}), which is due to the X_{e1h1} level splitting, while there is no absorption doublet from the X_{e1h2} level splitting simply because the X_{e1h2} absorption is optically forbidden for (symmetric) single QWs [i.e., Eq. (A13) gives $\chi^{(1)}_{X'G}(\omega)=0$, with $X'=X_{e1h2}$], although the X_{e1h2} level does split [according to Eq. (A15)].

In single QWs,[21] no Coulombic coupling occurs between excitons X_{e1h1} and X_{e1h2}, as the Coulomb matrix elements [given by Eq. (3)] associated with the e-h subband pairs, $(e1,h1)$ and $(e1,h2)$, are zero, i.e., $V_{1121}(q)=V_{1112}(q)=0$. Similarly, there is no CC between excitons X_{e1h1} and X_{e2h1}. In the ADQW considered here CC occurs between X_{e1h1} and X_{e2h1} due to the nonzero Coulomb matrix elements, $V_{1211}(q)$ and $V_{2111}(q)$, associated with the two e-h subband pairs, $(e1,h1)$ and $(e2,h1)$. This means that not only is the motion of each exciton in the QW growth direction and in the layer plane inseparable, but also the two exciton states of X_{e1h1} and X_{e2h1} couple. That is, the two *simplified* exciton wave functions, ψ's, mix to form two new wave functions corresponding to two *coupled*-exciton states. This coupling is indeed contained in the polarization equation [Eq. (5)] where interband polarization components associated with different e-h subband pairs couple through the Coulomb interaction. Below, when CC is taken into account, the symbol X_{enhl} is then interpreted as the coupled exciton the major component of which is associated with the e-h subband pair (en,hl). The calculated absorption coefficient when the CC is included is shown in Fig. 1(b) (*right-hand* column of graphs). Without a THz field (bottom panel), taking into account the CC slightly redshifts the dominant absorption at the X_{e1h1} energy (by about 0.6 meV), which is considerably enhanced in magnitude, whereas the absorption at X_{e2h1} is weakened and disappears in the broad continuum. This is in agreement with the result of previous calculations that the presence of higher-energy transitions enhances the absorption of lower-energy excitons due to CC.[32] The exciton absorption is determined by its oscillator strength which, for ideal 2D excitons, is proportional to $|\phi_s(\boldsymbol{\rho}=0)|^2$.[25] Hence, our result implies that the CC has caused a transfer of oscillator strength from the higher-energy coupled exciton, X_{e2h1}, to the lower-energy coupled exciton, X_{e1h1}. The X_{e2h1} absorption can be ascertained by removing the strong $h1$-$e1$ transitions in the calculation, and the dashed line (in the right bottom figure) shows the result after enlarging by six times. In addition to the X_{e2h1}

peak, there emerges a lower-energy peak at the energy position of X_{e1h1}, which is denoted as C_{e1h1}. The occurrence of C_{e1h1} reflects the CC between excitons X_{e1h1} and X_{e2h1}. It arises due to the $h1$-$e2$ transitions but is located at the X_{e1h1} energy. For simplicity C_{e1h1} is referred to as the Coulombic replica of exciton X_{e1h1}. However, the Coulombic replica of exciton X_{e2h1} is found to be an absorption dip rather than a peak at the position of X_{e2h1} when only the $h1$-$e1$ absorption is calculated (not shown). For the coupled exciton at the lower energy, X_{e1h1}, a small portion of its oscillator strength is due to X_{e2h1}. That is, due to CC a small amount of oscillator strength is shifted from the energetically higher transitions to the low-energy side, thus causing the transfer of oscillator strength to the lower-energy coupled exciton. In addition, comparing the two figures on the bottom panels, it is clear that the overall absorption is enhanced when the CC is taken into account. Similar results have been obtained from excitonic Green's-function calculations for CDQWs (Ref. 17) and shallow single QWs,[33] yielding good agreement with measurement.[17,33] Further, the effects of CC on the exciton energies and oscillator strengths have been studied recently for ADQWs.[16] It was found that excluding CC leads to the underestimation of the oscillator strength. The results reported here agree with this finding. As the energy positions of excitons X_{e1h1} and X_{e2h1} have slightly shifted from their positions in the Coulomb decoupling case, now the THz fields resonant with the exciton energy levels occur at the frequency of f=3.8 THz. Thus, absorption spectra for f=3.6, 3.8, 4.0 THz are shown to correspond with the f=3.4, 3.6, 3.8 THz spectra in the Coulomb decoupling case. Clearly the AT splitting of exciton X_{e1h1} survives the Coulombic coupling. The on-resonance spectrum shows symmetric X_{e1h1} doublets, but the splitting is slightly narrowed (by 0.35 meV) compared to the Coulomb decoupling case. The splitting of X_{e2h1} is not apparent and is only visible after the X_{e1h1} absorption is removed, as shown by the dashed line. Comparing the two columns of figures [Figs. 1(a) and 1(b)] for the various THz frequencies, we find that the effect of the CC is similar to the zero THz-field case: the overall absorption is enhanced, and in particular the enhancement at the lower-energy exciton X_{e1h1} is pronounced. This is again because (i) when the CC is taken into account, the excitonic oscillator strengths are accurately calculated and increased, and (ii) the CC leads to a shift of oscillator strength to the lower-energy exciton.

The question of what happens to the linear absorption if the THz frequency is low compared to the frequency separation of excitons X_{e1h1} and X_{e2h1} is considered next. To look into this, we calculated the interband absorption spectra in the presence of low-frequency THz fields. Calculations were performed excluding and including the CC, and the results for f=1 THz (THz-photon energy $\hbar\Omega$=4.136 meV) are shown in Figs. 2(a) and 2(b), respectively. Absorption at two high THz intensities of 3 and 6 MW/cm^2 (corresponding to the THz-field strengths of 21 and 29.7 kV/cm in the ADQW) is plotted together with the absorption without THz field. In both figures the X_{e1h1} peak is increasingly redshifted and decreases in magnitude with increasing THz-field strength while X_{e2h1} is blueshifted. Clearly features emerge about the dominant X_{e1h1} peak as well as the X_{e2h1} peak. To find out

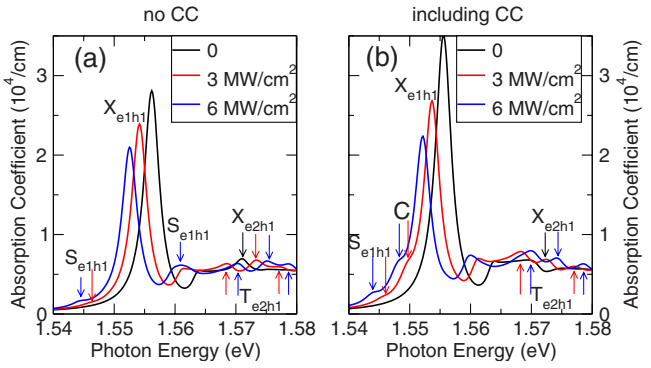

FIG. 2. (Color online) Interband absorption coefficients vs NIR photon energy at f=1 THz for three THz field intensities of 0, 3, and 6 MW/cm^2 for the cases of (a) excluding and (b) including CC. The same three subbands are adopted in the calculation as in Fig. 1.

where these features come from, we need to separate and check contributions to the absorption from the $h1$-$e1$ and the $h1$-$e2$ transitions respectively. For example, by setting zero to the dipole matrix elements for the $h1$-$e2$ transitions, we then obtain absorption in the presence of the THz fields due to the $h1$-$e1$ transitions only. Note that the X_{e2h1} exciton state remains but the transition to it from the ground state is intentionally set to be optically forbidden (i.e., X_{e2h1} is turned into a dark exciton). In Figs. 3(a) and 3(b) we show the results of the $h1$-$e1$ (dashed line) and the $h1$-$e2$ (dotted line) absorption in the more intense THz field, I_T=6 MW/cm^2, without and with CC included, respectively. The down (up) arrows are added pointing to the energies where the features emerge in the $h1$-$e1$ ($h1$-$e2$) absorption apart from the main exciton peak. For comparison the total absorption when both $h1$-$e1$ and $h1$-$e2$ transitions are taken into account (solid line) are also shown in the same figures. The $h1$-$e2$ absorption is weak so it is enlarged by ten times for clarity.

We first examine the case without Coulombic coupling. Comparing the $h1$-$e1$ absorption with the total absorption

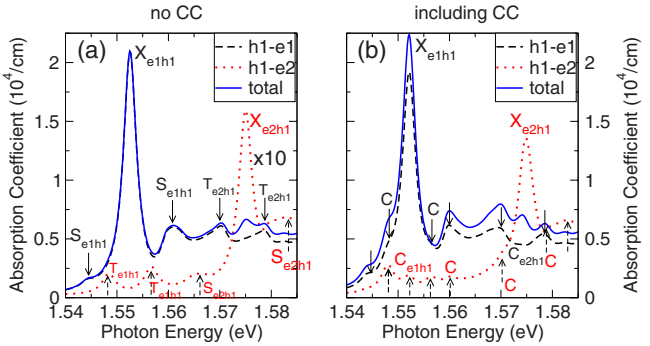

FIG. 3. (Color online) Interband absorption coefficients vs NIR photon energy at f=1 THz and THz field intensity of 6 MW/cm^2 due to the $h1$-$e1$ transitions (dashed line), the $h1$-$e2$ transitions (dotted line), and both $h1$-$e1$ and $h1$-$e2$ transitions (solid) for (a) excluding and (b) including CC. The down (up) arrows point to the features in the $h1$-$e1$ ($h1$-$e2$) absorption apart from the main exciton peak. The same three subbands are adopted in the calculation as in Fig. 1.

spectrum, we see that the two clear features around the X_{e1h1} exciton result from the band-to-band transitions, $h1$-$e1$. They are located at two THz-photon energy, $\pm 2\hbar\Omega$, from the main X_{e1h1} peak and are very weak in magnitude compared with the main peak. The two features are identified as the two two-THz-photon sidebands of the X_{e1h1} absorption due to the second-order Stark effect and occur in the interband absorption at *low-frequency* driving fields. They correspond to the absorption of the two excitonic components of X_{e1h1}, which are energetically nearest to its principal component (yielding the X_{e1h1} peak). This assignment is based on the proof given in Appendix, Sec. 2 and the following numerical verification. The energy separation $\hbar\omega_{X'X}$ between the exciton energy levels of X_{e1h1} and X_{e2h1} is about 14.5 meV. Using the dipole matrix element value $|\xi|=33.2$ eÅ inferred above, we find the Rabi energy $\hbar\Omega_R=4.9$ meV for the higher THz-field intensity of 6 MW/cm^2. Therefore, the requisite condition for the SOSE, i.e., $\Omega_R \ll \omega_{X'X}$ is satisfied. With no CC, X_{e1h1} and X_{e2h1} are well-defined excitons (i.e., no mixing occurs between them). Then the two exciton states plus the ground-state form a three-level system, which facilitates the check of our calculated spectral features against those expected from the SOSE. In SOSE the redshift in energy of the lower-energy main resonance, i.e., the X_{e1h1} energy level, is given by $2\hbar\Omega_R^2/\omega_{X'X}$, which gives 1.6 and 3.3 meV for THz-field intensities of 3 and 6 MW/cm^2, respectively. Figure 2(a) shows that the energy redshifts are 1.9 and 3.6 meV for the two THz intensities, in agreement with the theoretical values. Besides, the redshift of X_{e1h1} and blueshift of X_{e2h1} have almost the same magnitude, for instance, each excitonic peak being shifted by about 2 meV at a THz-field intensity of 3 MW/cm^2 with respect to the zero THz-field case [Fig. 2(a)]. We also verified numerically that the redshift values given above, 1.6 and 3.3 meV, are roughly half the dc Stark shifts in the dc fields of the same THz-field intensities of 3 and 6 MW/cm^2. For simplicity the SOSE sidebands of the X_{e1h1} exciton are denoted as S_{e1h1}. We see from Fig. 3(a) that clearly the two features around the X_{e2h1} exciton arise from the $h1$-$e1$ transitions (as the X_{e1h1} peak does). They are located at plus or minus one THz-photon energy $\pm\hbar\Omega$ from X_{e2h1}. As proved in the Appendix, they occur also due to the SOSE: the two resonances correspond to the two energy levels associated with the X_{e1h1} exciton but are formed near the X_{e2h1} level (located at $\pm\hbar\Omega$ from X_{e2h1}) due to the THz field. Therefore, these two features are simply the two single THz-photon replicas of X_{e2h1}, i.e., T_{e2h1}. We note that the lower-energy T_{e2h1} replica survives higher THz frequencies but shifts to the red and, as the THz frequency approaches the resonance frequency, it evolves into the *higher-energy* AT doublet of X_{e1h1} [as shown in Fig. 1(a)]. The two T_{e2h1} replicas [Fig. 3(a)] are offset from X_{e2h1} by one THz-photon energy. Further increasing the THz-field intensity (to 12 MW/cm^2, for instance), two more T_{e2h1} replicas emerge on the $h1$-$e1$ absorption curve offset from X_{e2h1} by *three* THz-photon energy, i.e., $\pm 3\hbar\Omega$. The excitonic sidebands of X_{e1h1} and the replicas of X_{e2h1} are two manifestations of the SOSE on the $h1$-$e1$ absorption. According to the Appendix, sidebands of X_{e2h1} and replicas of X_{e1h1} should occur as well due to the SOSE. This is indeed true, as we see from Fig. 3(a) that the features labeled with S_{e2h1} and T_{e1h1} appear on the dotted curve. However, these SOSE sidebands are very small in magnitude, as compared to the replicas of X_{e2h1} in the same energy region, thus making the latter dominant in the spectrum [Fig. 2(a)]. In the spectral region about the X_{e1h1} peak, the two replicas of X_{e1h1} are also weak so the SOSE sidebands of X_{e1h1} dominate the total absorption spectrum there. The $h1$-$e1$ transitions dominate the total absorption because they have much larger optical dipole matrix elements than the $h1$-$e2$ transitions ($|\mu_{11\mathbf{k}}| \approx 3|\mu_{21\mathbf{k}}|$). In near-resonance THz fields the higher-energy T_{e1h1} replica turns into the *lower-energy* AT doublet of X_{e2h1} [as shown in Fig. 1(a)].

We now proceed to analyzing the results in Fig. 2(b) for the case of including CC, by examining the respective contributions to the absorption from the $h1$-$e1$ and the $h1$-$e2$ transitions, which are shown in Fig. 3(b). Clearly there are features around each exciton peak at energies which are one and two THz-photon energy from the exciton energy, in the $h1$-$e1$ absorption spectrum (dashed line) as well as the $h1$-$e2$ absorption spectrum (dotted line). These features are located with respect to the exciton peak in the manner of sidebands due to the first-order Stark effect. However, the exciton peaks are significantly shifted in the THz fields: the X_{e1h1} absorption still shifts to the red while the X_{e2h1} absorption shifts to the blue, and the magnitudes of the shifts are similar to those in the Coulomb decoupling case [comparing Figs. 2(a) and 2(b)]. The shifts in these main absorption peaks in the presence of the THz fields do not arise from the FOSE [see the last paragraph of the Appendix]. Therefore, we rule out FOSE as being responsible for the features in Fig. 2(b). As has been verified above, the redshift and blueshift are in good agreement with those expected from the SOSE. On this basis the absorption still derives from the SOSE. Now the question is how does the SOSE occur with adjacent sidebands separated from each other by one rather than two THz-photon energy? The key to resolving this is the Coulombic coupling. Owing to CC, mixing occurs between the simplified wave functions ψ's of the two excitons, X_{e1h1} and X_{e2h1}, resulting in a Coulombic replica of exciton X_{e1h1}, namely, C_{e1h1} in the zero THz-field spectrum [the bottom graph of Fig. 1(b), dashed line]. When the THz field is turned on, this C_{e1h1} peak remains and shifts together with X_{e1h1} to the red, as can be seen from Fig. 3(b) (dotted line). The CC between the two excitons manifests itself in that the $h1$-$e1$ and $h1$-$e2$ polarization components, $p_{11\mathbf{k}}$ and $p_{12\mathbf{k}'}$, couple via the Coulomb matrix elements, $V_{1211}(|\mathbf{k}-\mathbf{k}'|)$ and $V_{2111}(|\mathbf{k}-\mathbf{k}'|)$ [Eq. (5)]. The $p_{12\mathbf{k}'}$ components giving rise to the two replicas, T_{e1h1} (around C_{e1h1}), on the $h1$-$e2$ absorption curve are connected to the $p_{11\mathbf{k}}$ components. As a result, at almost the same energies of the T_{e1h1} replicas two features about the X_{e1h1} peak arise on the $h1$-$e1$ absorption curve, labeled C due to the CC. They are not the FOSE sidebands of X_{e1h1} despite both features being just $\pm\hbar\Omega$ from X_{e1h1}. On the other hand, the SOSE sidebands of X_{e1h1} result from the $h1$-$e1$ polarization components $p_{11\mathbf{k}}$, which are connected to the $h1$-$e2$ polarization components $p_{12\mathbf{k}'}$ through the CC. We see then Coulombic features emerge in the $h1$-$e2$ absorption as well, at similar energies to the S_{e1h1} sidebands, e.g., the one at 1.56 eV (labeled C). Therefore, the complex absorption around the X_{e1h1} peak in Fig. 2(b) consists of the SOSE

sidebands and the THz-photon replicas of X_{e1h1}, as well as the Coulombic features derived from them. In fact at similar energy positions to these sidebands and replicas, absorption occurs also in the Coulomb decoupling case [compare Figs. 3(a) and 3(b)]. The difference is that without CC the two replicas, T_{e1h1}, are too weak to emerge from the total absorption. In other words, due to the CC the total absorption at the T_{e1h1} energy positions, in particular the absorption below X_{e1h1}, is significantly enhanced. A similar CC effect also occurs on the high-energy region around X_{e2h1}. The total absorption at the energies of T_{e2h1} is significantly enhanced, making the absorption at 1.57 eV even stronger than the X_{e2h1} peak.

Previous work has shown that excitonic absorption with "replicas"[34] occurs when a THz field drives a single QW.[22] Under additional dc bias, the QW is turned into an asymmetric QW. Just like the excitonic system considered above, a low-frequency THz field couples two exciton states of X_{e1h1} and X_{e1h2}. It is now clear, after the discussion in the preceding paragraphs, that the results of Ref. 22 can be well explained and all the replicas reported in that work can be explained in terms of CC and the SOSE without invoking the FOSE. The mechanism presented here not only explains the spectral positions of all the replicas and their bias dependence but can also describe their evolution with the frequency and intensity of the THz radiation. Furthermore, it is unifying and can explain the effects of THz fields on the interband absorption spectrum of any QW structure, symmetric or asymmetric. The subsequent discussion of the number of subbands contributing to the CC supports this assertion.

Having investigated the interband absorption in the ADQW involving three subbands (two electron subbands and one hole subband), we now proceed to exploring absorption involving more subbands. Experimentally the excitonic absorption without THz field can be obtained from the photoluminescence excitation (PLE) spectrum[2] or the reflectivity measurement.[6,27] The near band-edge PLE spectrum of the ADQW considered has been measured using a tunable cw-NIR probe.[2] Numerical calculation indicates that the third electron subband $e3$ is 110 meV higher than the second electron subband $e2$ and contributes to the interband absorption only at high photon energies (>1.7 eV). Therefore in this study we only need to consider the absorption to the lowest two electron subbands. The second hole subband $h2$ is separated from the first hole subband $h1$ by about 2 meV, while the third hole subband $h3$ is about 35 meV higher than subband $h2$. Thus, subbands $h2$ and $h3$ need to be considered. In the ADQW then there are six optically active excitons: X_{e1h1}, X_{e1h2}, X_{e2h1}, X_{e2h2}, X_{e1h3}, and X_{e2h3}. The calculated interband absorption without THz field is shown in the bottom two graphs in Fig. 4. The absorption peaks of the three excitons, X_{e1h1}, X_{e1h2}, and X_{e2h2}, are clearly seen at the photon energies of 1.5555, 1.5613, and 1.5695 eV, respectively, whereas the X_{e2h1} absorption is weak and peaks at 1.5712 eV. These energies can be interpreted as the energies of the four coupled excitons. Then the binding energy of exciton X_{enhl} can be given as the energy difference between the band-to-band transition energy, $\varepsilon_n^e+\varepsilon_l^h+E_g$, and the energy of exciton X_{enhl}. The calculated binding energies of these four excitons are 10, 6, 9, and 5 meV, respectively. X_{e1h1} and X_{e2h2} have large

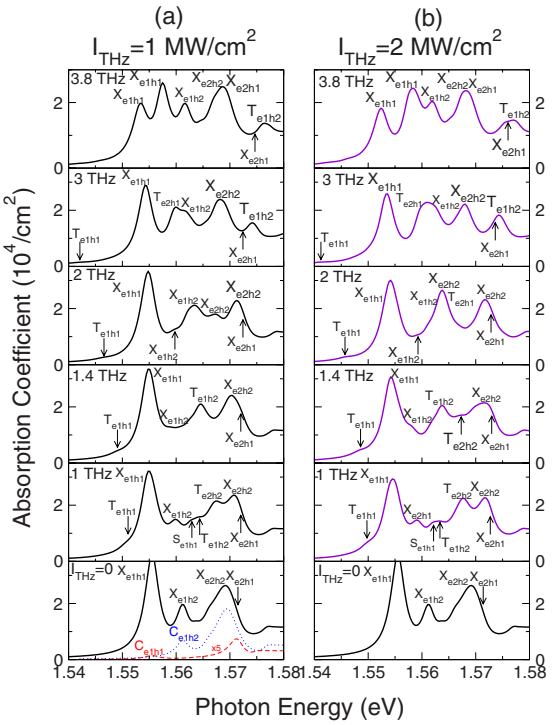

FIG. 4. (Color online) Interband absorption coefficients vs NIR photon energy from $f=1$ to 3.8 THz, as labeled in the panels, for THz field intensities of (a) 1 and (b) 2 MW/cm^2, in the ADQW with CC fully included. The bottom two graphs show the interband absorption with no THz field. The contribution to the absorption from the $h1$-$e2$ transitions (dashed line, $\times 5$) and that from the $h2$-$e2$ transitions (dotted line) are also shown in the left bottom figure.

binding energies, compared with X_{e1h2} and X_{e2h1}, as the Coulomb matrix elements [proportional to the form factors, Eq. (3)] $V_{1111}(q)$ and $V_{2222}(q)$ are much larger than $V_{1122}(q)$ and $V_{2211}(q)$ [see Fig. 5(a)]. X_{e2h2} has a larger binding energy than X_{e2h1}, making X_{e2h2} appear energetically lower than X_{e2h1}. Excitons X_{e1h3} and X_{e2h3} are located at even higher energies (1.589 and 1.604 eV, respectively), both being connected to hole subband $h3$. Both these excitons have too small oscillator strengths (which are only $\sim 1\%$ of the X_{e1h2}'s oscillator strength) to give rise to appreciable absorption.

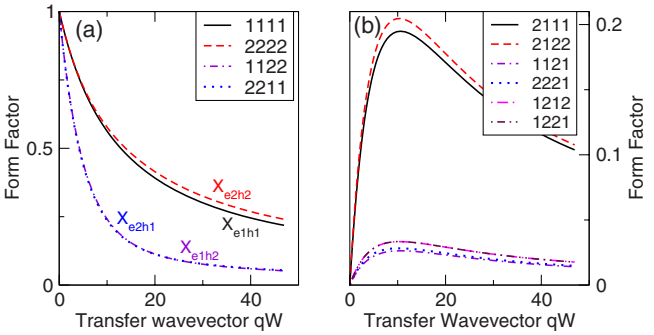

FIG. 5. (Color online) Form factors $\mathcal{F}_{n'nl'l}$ [Eq. (4)] vs the dimensionless transfer wave vector (lines are labeled with $n'nl'l$) for (a) the four excitons X_{e1h1}, X_{e1h2}, X_{e2h2}, X_{e2h1} and (b) the Coulombic coupling between any two of the four excitons.

Overall, the calculated absorption spectrum has clearly reproduced all the exciton absorption features of the PLE spectrum [compared to Fig. 1(b) of Ref. 2]. In what follows we confine ourselves to the four low-energy excitons that dominate the absorption and study the influence of THz fields on the excitonic absorption for the NIR photon energies as in the PLE spectrum.[2] Now, the electronic system we consider essentially consists of five energy states, namely, the four exciton states X_{e1h1}, X_{e1h2}, X_{e2h2}, and X_{e2h1} plus the ground state. Owing to inversion asymmetry, complications arise from the CC between any two of the four excitons. The excitonic Coulombic coupling can be categorized into three types according to the electron and hole subbands involved. The *first* type of CC occurs between two excitons which are associated with the different electron subbands, namely, $e1$ and $e2$ but the same hole subband, $h1$ or $h2$. That is, X_{e1h1} and X_{e2h1} couple, and X_{e1h2} and X_{e2h2} couple. In the left bottom graph of Fig. 4, we also plot the absorption spectra due to the $h1$-$e2$ transitions only (dashed line, enlarged by five times) and the $h2$-$e2$ transitions only (dotted line). The presence of the Coulombic replicas, C_{e1h1} and C_{e1h2}, is evidence of the CC between the two excitons, X_{e1h1} and X_{e2h1}, and between X_{e1h2} and X_{e2h2}. The CC between the former pair of excitons is due to the two nonzero Coulomb matrix elements $V_{1211}(q)$ and $V_{2111}(q)$ [Eqs. (3) and (4)], whereas the CC between the latter pair is due to the nonzero $V_{1222}(q)$ and $V_{2122}(q)$. The C_{e1h2} peak is 22 times higher than the C_{e1h1} peak, not just because the CC is stronger between excitons X_{e1h2} and X_{e2h2} than between X_{e1h1} and X_{e2h1}, but also because the $h2$-$e2$ transitions have three times as large interband dipole matrix elements as the $h1$-$e2$ transitions. In the $h1$-$e1$ ($h2$-$e1$) absorption spectrum (not shown) the Coulombic replica of exciton X_{e2h1} (X_{e2h2}) appears to be an absorption dip at the energy position of X_{e2h1} (X_{e2h2}). The *second* type of CC exists between two excitons which connect with interband transitions from different hole subbands to the same electron subband, namely, between X_{e1h1} and X_{e1h2}, and between X_{e2h1} and X_{e2h2}. The coupling is however very weak compared to the first type of CC. This is because the Coulomb matrix elements that are responsible, $V_{1112}(q)$, $V_{1121}(q)$, $V_{2212}(q)$, and $V_{2221}(q)$, are very small compared to the four Coulomb matrix elements in the first type of CC, as can be seen from the following proof. Of the eight Coulomb matrix elements, according to Eqs. (3) and (4), only four are independent because of the complex conjugate relations, namely, $V_{2111}(q)=V^*_{1211}(q)$, $V_{2122}(q)=V^*_{1222}(q)$, $V_{1121}(q)=V^*_{1112}(q)$, and $V_{2221}(q)=V^*_{2212}(q)$. To compare the magnitudes of these Coulomb matrix elements, therefore, we only need to plot the absolute values of four form factors, for example, $|\mathcal{F}_{2111}(q)|$, $|\mathcal{F}_{2122}(q)|$, $|\mathcal{F}_{1121}(q)|$, and $|\mathcal{F}_{2221}(q)|$, as functions of the transfer wave vector q, as shown in Fig. 5(b). Clearly we see that $|\mathcal{F}_{1121}(q)|$ and $|\mathcal{F}_{2221}(q)|$ are much smaller than $|\mathcal{F}_{2111}(q)|$ and $|\mathcal{F}_{2122}(q)|$, with $|\mathcal{F}_{2122}(q)|$ being larger than the rest. Both $|\mathcal{F}_{1121}(q)|$ and $|\mathcal{F}_{2221}(q)|$ are small because the hole envelope functions $g_1(z_h)$ and $g_2(z_h)$ in the integrand of the form factors [Eq. (4)] have small overlap. In both types I and II CC, when a THz field is applied a dipole moment can be induced between a pair of Coulomb-coupled excitons via the interaction with the THz field. The *third* type of CC occurs between two excitons which are connected to the different electron subbands, $e1$ and $e2$, and different hole subbands, $h1$ and $h2$. That is, there is CC between excitons X_{e1h1} and X_{e2h2}, and between excitons X_{e1h2} and X_{e2h1}, due to the nonzero Coulomb matrix elements, $V_{1212}(q)$, $V_{2121}(q)$, $V_{1221}(q)$, and $V_{2112}(q)$ [only two matrix elements are independent as the first (last) two are complex-conjugate related]. However, these Coulomb matrix elements are very small (similar to the second type of CC), as can be seen from the form factors $|\mathcal{F}_{1212}(q)|$ and $|\mathcal{F}_{1221}(q)|$ in Fig. 5(b). The result that types II and III CC are weak allows only type I CC to be considered when analyzing the intricate effects of THz fields on absorption.

Unlike the three-level system, seeking analytical solutions for absorption resonances in the five-level system is a formidable task. Therefore, we calculated interband absorption coefficient for THz fields at a number of THz frequencies to reveal the details as the absorption evolves with the THz frequency. The results are shown in Figs. 4(a) and 4(b) for two THz-field intensities of 1 and 2 $\mathrm{MW/cm^2}$, respectively, at several THz frequencies as indicated (up to 3.8 THz). The intensity of 2 $\mathrm{MW/cm^2}$ (corresponding to the THz electric-field strength of 17 kV/cm in the ADQW) is approximately the highest intensity of tunable THz radiation from free-electron lasers (full THz power is about 2 kW).[2] The identification of the excitonic features is based on the numerical calculations and is labeled using the same notation as above for the three-level system. There are Coulombic replicas at photon energies where the exciton absorption occurs. Similarly Coulombic features occur as well at energies of the strong excitonic sidebands and THz-photon replicas. These Coulombic replicas and features are not labeled for clearness. The intersubband dipole matrix element associated with $h1$ and $h2$, ζ_{12}, is small being only one fifth of ξ_{12}, the dipole matrix element associated with the $e1$ and $e2$ subbands. Therefore, the THz-field-induced intersubband transitions between the electron subbands dominate over those between the hole subbands. At the low frequency $f=1$ THz, the X_{e1h1} and X_{e1h2} energies shift to the red while the two higher-energy excitons X_{e2h2} and X_{e2h1} shift to the blue. This is due to the low-frequency Stark effect (Appendix). As the intersubband transitions between the *electron* subbands are dominant, the THz field interacts strongly with excitons X_{e1h2} and X_{e2h2}, as well as excitons X_{e1h1} and X_{e2h1}, the energy levels of each pair having a large interval compared to the THz-photon energy. Apart from the exciton peaks, four other features are visible due to the THz field-exciton interaction. The two features—labeled S_{e1h1} and T_{e1h1}—are, respectively, the SOSE sideband and replica of exciton X_{e1h1} and are not new having featured in the three-level system [Fig. 3(a)]. The other two features at photon energies of about 1.564 and 1.567 eV, T_{e1h2} and T_{e2h2}, are the THz-photon replicas of excitons X_{e1h2} and X_{e2h2}, respectively. They arise due to the dipole interaction between the THz field and the excitons and are, respectively, located at one THz-photon energy higher than X_{e1h2} and lower than X_{e2h2}. Interestingly the T_{e2h2} feature is comparable in magnitude to the X_{e2h2} peak. The fact that these sidebands and replicas feature in the absorption spectrum is also a consequence of the great strength of the electron intersubband transitions compared to the hole intersubband transitions. However, these are not the only features

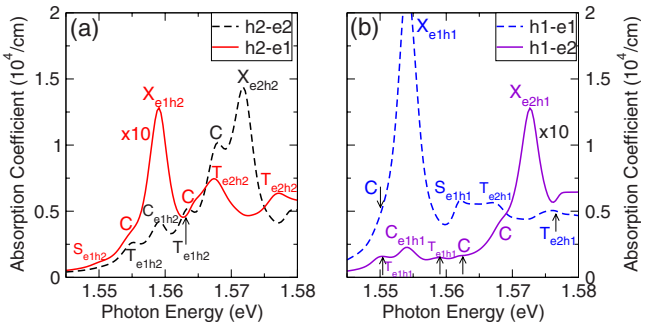

FIG. 6. (Color online) Interband absorption coefficients vs NIR photon energy at $f=1$ THz and THz field intensity of 2 MW/cm^2 with CC included due to (a) the $h2$-$e1$ transitions (solid line, $\times 10$) and the $h2$-$e2$ transitions (dashed line) and (b) the $h1$-$e1$ transitions (dashed line) and the $h1$-$e2$ transitions (solid line, $\times 10$).

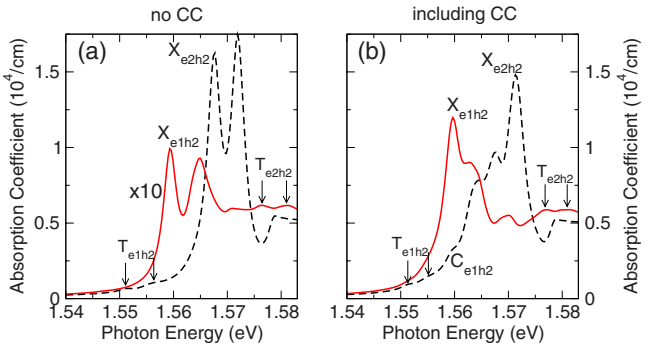

FIG. 7. (Color online) Interband absorption coefficients vs NIR photon energy at $f=2$ THz and THz field intensity of 1 MW/cm^2 due to the $h2$-$e1$ transitions (solid line, $\times 10$) and the $h2$-$e2$ transitions (dashed line) for (a) excluding and (b) including CC.

that occur. There are also others which can be seen more clearly in the individual hole subband to electron subband absorption. As a typical illustration, Figs. 6(a) and 6(b) show the absorption due to the $h2$-$e1$ and $h2$-$e2$ transitions, and the absorption due to the $h1$-$e1$ and $h1$-$e2$ transitions, respectively, with the CC included for the THz field intensity of 2 MW/cm^2. The $h2$-$e1$ and $h1$-$e2$ absorption is small and enlarged by ten times. Besides the exciton peaks and SOSE replicas, the SOSE sidebands, S_{e1h1} and S_{e1h2}, the Coulombic replicas, C_{e1h1} and C_{e1h2}, and the Coulombic features (labeled C) derived from the SOSE sidebands and replicas are also present. In both figures the features from Coulombic coupling occur at the photon energies where the SOSE sidebands or replicas are strong. For example, in Fig. 6(a) a strong Coulombic feature emerges at 1.5680 eV on the $h2$-$e2$ absorption curve, coincident with a strong T_{e2h2} replica in the $h2$-$e1$ absorption. The Coulombic features are stronger in Fig. 6(a) than Fig. 6(b), since $|V_{2122}(q)|>|V_{2111}(q)|$ [refer to Fig. 5(b) above]. The C_{e1h2} peak is 18 times higher than the C_{e1h1} peak, similar to the case of no THz field [refer to Fig. 4(a), left bottom panel].

The $f=1.4$ THz fields are resonant with the two excitons, X_{e1h1} and X_{e1h2}. However, no splitting is found for either exciton peak for two reasons. First, the THz-field-induced transition between the two exciton states is determined by the intersubband transition between the two hole subbands $h1$ and $h2$, which is not favored compared to the electron intersubband transitions between $e1$ and $e2$. The T_{e1h2} replica results from the dipole interaction between the THz field and the excitons X_{e1h2} and X_{e2h2}. The presence of the strong T_{e1h2} replicas in the figure implies that the $e1$-$e2$ transitions are still dominant, even when the THz field is resonant with the $h1$-$h2$ intersubband transitions. Second, the splitting is estimated to be 0.9 meV in the high intensity THz field of 2 MW/cm^2. As this value is smaller than the homogeneous linewidth, $2\hbar\gamma_p=2$ meV, due to dephasing, no splittings emerge. The $f=2$ THz fields are resonant with excitons X_{e1h2} and X_{e2h2}. Now we find that both exciton peaks each have split into two AT doublets. For example, there two peaks of the exciton X_{e2h2} are clearly resolved but are very asymmetric in magnitude. Three clear absorption peaks are developed on the $I_{THz}=2$ MW/cm^2 graph, where the middle peak consists of three features which roughly coincide, namely, the upper AT doublet of X_{e1h2}, the lower AT doublet of X_{e2h2}, and the THz-photon replica of X_{e2h1}, i.e., T_{e2h1}. To investigate the CC effects on the absorption, Fig. 7(b) shows the absorption in the THz field of intensity 1 MW/cm^2 due to the respective $h2$-$e1$ and $h2$-$e2$ transitions, calculated with the CC included, compared with the absorption without the CC in Fig. 7(a). In both figures $h2$-$e1$ absorption is enlarged by ten times. With no CC there is a clear double peak with close magnitudes in each of the $h2$-$e1$ and $h2$-$e2$ absorption spectra. When the CC is taken into account, however each pair of doublets become highly asymmetric in strength with the energy splittings slightly narrowed. The strength of the X_{e2h2} doublets is significantly weakened, while two Coulombic sidebands of X_{e1h2} emerge at the energies of the X_{e1h2} doublets. This indicates that, due to the CC, some of the oscillator strength of the higher-energy exciton X_{e2h2} is transferred to the lower-energy coupled exciton X_{e1h2}. It is then not surprising that in $h2$-$e1$ absorption, when the CC is included, the absorption of the lower-energy doublet of X_{e1h2} is significantly enhanced as the oscillator strength of X_{e1h2} is increased. Therefore, in Fig. 4 the absorption doublets of each exciton are in essence still Autler-Townes doublets but now they have very distinct strengths.

This high asymmetry of the AT doublets is quite different from the X_{e1h1}-X_{e2h1} excitonic mixing case, where the on-resonance spectrum shows nearly symmetric doublets [see Fig. 1(b)]. To explain this we first compare the absorption of the two "single" excitons X_{e1h2} and X_{e2h2}, i.e., ignoring the excitonic mixing. The absorption of the X_{e2h2} doublets is more than one order of magnitude stronger than the absorption of the X_{e1h2} doublets [Fig. 7(a)] since (i) the interband dipole matrix elements $|\mu_{22\mathbf{k}}|\approx 3|\mu_{12\mathbf{k}}|$ and (ii) the Coulomb matrix elements $|V_{2222}(q)|>|V_{1122}(q)|$. This means that the X_{e2h2} doublets have very large oscillator strength compared to the lower-energy X_{e1h2} doublets. Including CC then causes a significant transfer of oscillator strength to increase significantly the absorption at the lower energies. Indeed, it is the Coulombic replicas C_{e1h2} [Fig. 7(b), dashed line] that dictate the total absorption at the lower energies in Fig. 4. The absorption in the higher-energy region is of course determined by the X_{e2h2} doublets. As a result, each pair of AT doublets is highly asymmetric. In contrast, in the X_{e1h1}-X_{e2h1} coupling

case, the oscillator strength of the higher-energy exciton X_{e2h1} is very small compared to the lower-energy exciton X_{e1h1}. Thus, the effect of CC on the absorption of both excitons is weak, making the AT doublets highly symmetric. We notice that, in the $h2$-$e2$ absorption [Figs. 7(a) and 7(b)], a pair of weak replicas, T_{e1h2}, appears in the low-energy region at positions one THz-photon energy lower than the X_{e1h2} doublets, respectively. Similarly in the $h2$-$e1$ absorption a pair of T_{e2h2} replicas emerges on the high-energy side and is located at one THz-photon energy higher than the X_{e2h2} doublets. These double replicas arise irrespective of CC. They occur because of the strong resonant interaction of the THz field with excitons X_{e1h2} and X_{e2h2}, similar to that in atoms.[11,12] However, they are too weak compared with the other exciton features to emerge from the total absorption in Fig. 4.

The THz fields with the frequency of 3 THz are 4.14 meV off resonance with the two excitons, X_{e1h2} and X_{e2h2}. We see from Fig. 4 that one doublet of X_{e2h2} is converted back to the THz-photon replica T_{e1h2}, but it now appears on the high-energy side of X_{e2h2} compared to the low side at $f=1.4$ THz. This replica-to-doublet and then doublet-to-replica conversion is similar to that which occurs to the three-level system as in Fig. 1(a). On the other hand, the $f=3$ THz fields are 3.3 meV below resonance with the excitons X_{e1h1} and X_{e2h1}. Therefore, as can be seen from both the $I_{THz}=1$ and 2 MW/cm^2 figures, the absorption of the THz-photon replica T_{e2h1} starts to strengthen and, with increasing THz frequency, evolves into the higher-energy AT doublet of X_{e1h1}. Finally, at $f=3.8$ THz the excitons, X_{e1h1} and X_{e2h1}, are exactly at resonance with the THz fields. We see both excitons split into the AT doublets. In fact the lower-energy doublet of X_{e2h1} has very similar strength to its higher-energy partner but is coincident in energy with the strong X_{e2h2} absorption. The X_{e1h1} doublets have similar strengths as well, and the small difference is due to the CC between excitons X_{e1h1} and X_{e2h1}, and absorption due to the other two excitons. The *double* peak of X_{e1h1} is very pronounced compared to the absorption doublets of X_{e1h2} or X_{e2h2} at $f=2$ THz. The reason for this has been pointed out above. The higher-energy exciton X_{e2h1} has very small oscillator strength compared with its lower-energy counterpart, X_{e1h1}. Thus, the transfer of oscillator strength from X_{e2h1} does not affect much the absorption of the X_{e1h1} AT doublets.

So far, we have paid no attention to the interaction of the THz fields with excitons X_{e1h1} and X_{e2h2}, and the interaction with X_{e1h2} and X_{e2h1}. In fact, these interactions are very weak even when taking CC into account because there have very small dipole matrix elements for the (THz-field-induced) transitions between each of the two pairs of exciton states [e.g., the matrix elements $\langle X_{e1h1}|\bar{e}z_e(ez_h)|X_{e2h2}\rangle$ are for the transitions between the X_{e1h1} and X_{e2h2} states]. Moreover, when the THz-field frequency is further increased to ~ 8 THz, excitons X_{e1h3} and X_{e2h3} are involved in the THz field-exciton interaction. The X_{e1h3} state is then coupled with the X_{e1h1} state by the high-frequency THz field. Since the high-energy exciton, X_{e1h3}, has very small oscillator strength ($<0.1\%$ of the X_{e1h1}'s oscillator strength), it hardly affects the X_{e1h1} absorption at the lower energies by transfer of its oscillator strength.

We now look again at the absorption spectra in Fig. 4 as a whole to see the spectral evolution with THz frequency. Basically the absorption of the X_{e1h1} and X_{e2h2} excitons and the THz-photon replicas of X_{e1h2} and X_{e2h1} dominate the absorption spectra because of the large oscillator strengths of the $h1$-$e1$ and $h2$-$e2$ transitions. However, the absorption of the X_{e1h2} exciton and the T_{e2h2} replica are also significant due to CC, although both are associated with $h2$-$e1$ transitions which are much weaker compared to the $h1$-$e1$ or $h2$-$e2$ transitions. In fact, we have tested for a range of THz frequencies that the inclusion of CC causes significant enhancement of the overall absorption, in particular the absorption on the low-energy side. The SOSE sidebands appear only at very low THz frequencies, but are very weak compared to the other features. The resonant frequency connecting to the two excitons, X_{e1h2} and X_{e2h2}, is 2 THz. Since the THz frequencies considered are around this resonance frequency, it is reasonable to find that two clear features connected with exciton X_{e2h2}, namely, the X_{e2h2} and T_{e1h2} peaks, are always present. The main X_{e2h2} absorption basically blueshifts at low THz frequencies and then shifts to the red with increasing the THz frequency. The X_{e1h1} absorption shifts to the red with the increase in the THz frequency until it splits at $f=3.8$ THz. As the THz frequency increases, clearly the absorption spectrum broadens with more peaks turning up.

IV. CONCLUSIONS

In conclusion, optical absorption in ADQWs in the presence of an intense THz field applied parallel to the growth direction has been studied by solving interband polarization equation numerically. It is shown that the influence of the THz field on the interband absorption is only accurately described when CC is taken into account. This is because CC occurs between excitons in ADQW structures, owing to the lack of inversion symmetry, in addition to the strong dipole interaction arising from the THz field. A rich variety of behaviors, including excitonic sidebands and replicas as well as peak splittings, is revealed in the absorption spectra. The behavior of the excitonic peak splittings and complexes and their variation with the THz field are well explained in terms of the CC and the Stark effects (OSE and SOSE) due to the THz field-exciton interaction. While the OSE and SOSE cause the excitonic peak splittings and breakups, the CC can significantly alter the intensities of the spectral components, and excitonic absorption connected with weak band-to-band transitions can occur with a great strength. When the THz field is near resonant with the energy levels of two excitons, AT splittings occur with the absorption of each exciton splitting into two peaks. This is due to the OSE: the resonant THz field-exciton interaction causes each excitonic level to split into two doublets. Due to Coulombic coupling, however, some of the oscillator strength of the higher-energy exciton is transferred to the doublets of the coupled lower-energy exciton. It is found that the large transfer of oscillator strength causes a pronounced asymmetry to each pair of AT absorption peaks. In a low-frequency driving THz field (i.e., the THz-photon energy is very small compared with the energy difference between the two excitonic levels), excitonic THz-

photon sidebands and replicas occur to each exciton and arise from different band-to-band transitions. The occurrence of the sidebands and replicas is proved to be due to the SOSE. These sidebands and replicas form multiple features, which are separated from the excitonic peak by both odd and even integer multiples of the THz-photon energy $n\hbar\Omega$ ($n=\pm1,\pm2,\pm3,\ldots$). Taking into account CC, the overall absorption, in particular the absorption on the low-energy side, is significantly enhanced for a wide range of THz frequencies.

ACKNOWLEDGMENT

The authors wish to thank the Engineering and Physical Sciences Research Council, U.K. for funding under Grant No. EP/D502241/1 "PORTRAIT."

APPENDIX: EXCITONIC ABSORPTION IN THZ-FIELD-DRIVEN QWS—A DENSITY-MATRIX DERIVATION

In order to analyze the numerical results we adopt a simplified model such that the density-matrix formalism can be applied to give analytical solutions of the optical susceptibility. The Hamiltonian is $H=H_0+H_\omega+H_\Omega$, where H_0 is the Hamiltonian of the unperturbed QW and H_ω (H_Ω) is the interaction of the QW with the NIR (THz) field $E_\omega=E_0\cos\omega t$ ($E_\Omega=E_T\cos\Omega t$). We confine ourselves to three energy levels: the ground state $|G\rangle$ and two exciton states $|X\rangle,|X'\rangle$ (let $\hbar\omega_X=E_X-E_G$, $\hbar\omega_{X'}=E_{X'}-E_G$, and $\hbar\omega_{X'X}=E_{X'}-E_X>0$). They constitute the simplest model system interacting with the two light fields. $\langle X|H_\omega|G\rangle=-\mu_X E_\omega$, $\langle X'|H_\omega|G\rangle=-\mu_{X'}E_\omega$, where μ_X ($\mu_{X'}$) is the dipole matrix element of exciton X (X'). $\langle X'|H_\Omega|X\rangle=-\xi_{X'X}E_\Omega$, where $\xi_{X'X}$ is the dipole matrix element connecting the two exciton states via the dipole interaction of the electron with the THz field. Note that μ_X is not to be confused with $\mu_{nl\mathbf{k}}$ (Sec. II): if $|X\rangle$ is expanded into the noninteracting e-h pair states $|n\mathbf{k},l\bar{\mathbf{k}}\rangle$ ($\mathbf{k}=-\bar{\mathbf{k}}$ is the 2D wave vector of the hole) as[23,24] $|X\rangle=\Sigma_{nl\mathbf{k}}F^X_{nl\mathbf{k}}|n\mathbf{k},l\bar{\mathbf{k}}\rangle$, μ_X is related to $\mu_{nl\mathbf{k}}$ via[23,35] $\mu_X=\Sigma_{nl\mathbf{k}}F^{X^*}_{nl\mathbf{k}}\mu_{nl\mathbf{k}}$. Similarly $\xi_{X'X}$ is related to $\xi_{n'n}$ via $\xi_{X'X}=\Sigma_{n'nl\mathbf{k}}F^{X'^*}_{n'l\mathbf{k}}F^X_{nl\mathbf{k}}\xi_{n'n}$.

Using Liouville's equation,[11] the equation of motion for the density matrix ρ is obtained. For weak NIR probe, we neglect the dynamics of ρ's diagonal elements ρ_{GG}, ρ_{XX}, and $\rho_{X'X'}$, as well as that of the off-diagonal elements connecting the two exciton states $\rho_{XX'}$ and $\rho_{X'X}$. Considering $\rho_{GX}=\rho^*_{XG}$, and $\rho_{GX'}=\rho^*_{X'G}$, we are left with two equations to describe the excitonic dynamics,

$$i\hbar\dot{\rho}_{XG}=\hbar\omega_X\rho_{XG}-\mu_X E_\omega(\rho_{GG}-\rho_{XX})-\xi_{XX'}E_\Omega\rho_{X'G}-i\hbar\gamma\rho_{XG}, \tag{A1}$$

$$i\hbar\dot{\rho}_{X'G}=\hbar\omega_{X'}\rho_{X'G}-\mu_{X'}E_\omega(\rho_{GG}-\rho_{X'X'})-\xi_{X'X}E_\Omega\rho_{XG}-i\hbar\gamma\rho_{X'G}, \tag{A2}$$

where $\dot{\rho}=\frac{\partial\rho}{\partial t}$ and γ is the dephasing rate. Using Floquet's theorem,[18,36] and in the rotating-wave approximation[26] with respect to the NIR probe, it is found that ρ_{XG} and $\rho_{X'G}$, the solution of Eqs. (A1) and (A2), have the form

$$\rho_{XG}(t)=e^{-i\omega t}\sum_{n=-\infty}^{+\infty}A_n e^{-in\Omega t},\quad \rho_{X'G}(t)=e^{-i\omega t}\sum_{n=-\infty}^{+\infty}B_n e^{-in\Omega t}. \tag{A3}$$

Following conventional notations,[11] we use a bracketed circular frequency to label the Fourier component of a light field [e.g., $E(\omega)\propto e^{-i\omega t}$] as well as that of an element of ρ [e.g., $\rho^{(|n|+1)}_{XG}(\omega+n\Omega)\propto e^{-i(\omega+n\Omega)t}$]. Only zero-order components are retained for ρ's diagonal elements (e.g., $\rho^{(0)}_{XX}$). Inserting Eq. (A3) into Eqs. (A1) and (A2) and using the orthogonality of the series, we find

$$(\omega+n\Omega-\omega_X+i\gamma)A_n+\frac{1}{2\hbar}\xi_{XX'}E_T(B_{n-1}+B_{n+1})=-\frac{1}{2\hbar}\mu_X E_0(\rho^{(0)}_{GG}-\rho^{(0)}_{XX})\delta_{n,0}, \tag{A4}$$

$$(\omega+n\Omega-\omega_{X'}+i\gamma)B_n+\frac{1}{2\hbar}\xi_{X'X}E_T(A_{n-1}+A_{n+1})=-\frac{1}{2\hbar}\mu_{X'}E_0(\rho^{(0)}_{GG}-\rho^{(0)}_{X'X'})\delta_{n,0}. \tag{A5}$$

This set of equations can be separated into two independent sets (below let k be any even integer and l any odd integer) as follows:

$$(\omega+k\Omega-\omega_X+i\gamma)A_k+\frac{1}{2\hbar}\xi_{XX'}E_T(B_{k-1}+B_{k+1})=-\frac{1}{2\hbar}\mu_X E_0(\rho^{(0)}_{GG}-\rho^{(0)}_{XX})\delta_{k,0}, \tag{A6}$$

$$(\omega+l\Omega-\omega_{X'}+i\gamma)B_l+\frac{1}{2\hbar}\xi_{X'X}E_T(A_{l-1}+A_{l+1})=0, \tag{A7}$$

for even A's and odd B's, and

$$(\omega+l\Omega-\omega_X+i\gamma)A_l+\frac{1}{2\hbar}\xi_{XX'}E_T(B_{l-1}+B_{l+1})=0, \tag{A8}$$

$$(\omega+k\Omega-\omega_{X'}+i\gamma)B_k+\frac{1}{2\hbar}\xi_{X'X}E_T(A_{k-1}+A_{k+1})=-\frac{1}{2\hbar}\mu_{X'}E_0(\rho^{(0)}_{GG}-\rho^{(0)}_{X'X'})\delta_{k,0}, \tag{A9}$$

for odd A's and even B's. These two sets of equations are general expressions and will be used below to deduce linear absorption in QWs driven by near-resonance or low-frequency THz fields.

1. Absorption in near-resonance THz fields: OSE and AT splitting

When a THz field is near resonance with levels E_X and $E_{X'}$, its detuning $\delta=\Omega-\omega_{X'X}$ is very small compared to $\omega_{X'X}$, i.e., $|\delta|\ll\omega_{X'X}$. To calculate first-order susceptibility one needs to solve for $\rho^{(1)}_{XG}(\omega)=A_0e^{-i\omega t}$ and $\rho^{(1)}_{X'G}(\omega)=B_0e^{-i\omega t}$. Take $k=0$ in Eq. (A6). As $|B_{-1}|\ll|B_1|$, we neglect the term $\propto B_{-1}$. Then setting $l=1$ in Eq. (A7) and discarding the term $\propto A_2$ ($|A_2|\ll|A_0|$), one expresses B_1 in terms of A_0. Substituting this expression into the former equation yields A_0. Thus, one obtains $\rho^{(1)}_{XG}(\omega)$, which contributes to the first-order susceptibility via $\chi^{(1)}_X(\omega)=\frac{2}{V}\mu^*_X\rho^{(1)}_{XG}(\omega)/E(\omega)$,

$$\chi^{(1)}_X(\omega)=-\frac{2}{V}\frac{1}{\mathcal{D}_X}\frac{1}{\hbar}|\mu_X|^2(\rho^{(0)}_{GG}-\rho^{(0)}_{XX})(\omega+\Omega-\omega_{X'}+i\gamma), \tag{A10}$$

where

$$\mathcal{D}_X=(\omega-\omega_X+i\gamma)(\omega+\Omega-\omega_{X'}+i\gamma)-\Omega_R^2. \tag{A11}$$

Here, $\Omega_R=\frac{1}{2}|\xi_{X'X}|E_T/\hbar$ is the Rabi frequency[11] for the THz field. The resonances of the absorption spectrum, $\alpha(\omega)\propto\mathrm{Im}\,\chi^{(1)}(\omega)$, are thus determined by $\mathrm{Re}\,\mathcal{D}_X=0$,

$$\omega=\omega_X+\tfrac{1}{2}(-\delta\pm\Delta), \tag{A12}$$

where $\Delta=[\delta^2+4(\gamma^2+\Omega_R^2)]^{1/2}$ is the THz-field-induced E_X level splitting. Equations (A10)–(A12) show that the original exciton absorption at ω_X (Ref. 23) now splits into two lines in the presence of a resonant THz field, at the two frequencies given by Eq. (A12). This is the AT splitting,[12] which was studied by solving the time-dependent wave equation for two-level atoms.

Similarly, by solving Eqs. (A8) and (A9) one finds B_0 and then obtains the susceptibility,

$$\chi^{(1)}_{X'}(\omega)=-\frac{2}{V}\frac{1}{\mathcal{D}_{X'}}\frac{1}{\hbar}|\mu_{X'}|^2(\rho^{(0)}_{GG}-\rho^{(0)}_{X'X'})(\omega-\Omega-\omega_X+i\gamma), \tag{A13}$$

where

$$\mathcal{D}_{X'}=(\omega-\omega_{X'}+i\gamma)(\omega-\Omega-\omega_X+i\gamma)-\Omega_R^2. \tag{A14}$$

Then we find the resonances of $\chi^{(1)}_{X'}(\omega)$ by requiring $\mathrm{Re}\,\mathcal{D}_{X'}=0$,

$$\omega=\omega_{X'}+\tfrac{1}{2}(\delta\pm\Delta). \tag{A15}$$

Equations (A10) and (A13) differ from the usual linear susceptibility in that the THz-field effect is included. Without THz field they simply reduce to the linear susceptibility[23] for exciton absorption in QWs, with resonances occurring at the exciton energies $\hbar\omega_X$ and $\hbar\omega_{X'}$.

2. Absorption in low-frequency THz fields: SOSE and FOSE

As we tackle the spectrum and frequency shift due to low-frequency THz fields ($e^{-i\Omega t}\sim 1$), we start with the dc field case and then modify the result to account for slowly varying field effects. This approach is similar to that adopted by Autler and Townes.[12] In the following deduction is made for the X excitonic absorption but solutions to the X' absorption can be sought similarly. For $\Omega=0$ (i.e., in dc field E_T) Eqs. (A1) and (A2) reduce to the equations of motion for $\rho^{(1)}_{XG}(\omega)$ and $\rho^{(1)}_{X'G}(\omega)$, respectively [i.e., only the A_0, B_0 coefficients in Eq. (A3) are nonzero]. Solving the equations yields

$$\rho^{(1)}_{XG}(\omega)=-\frac{1}{\mathcal{D}_0}\frac{1}{\hbar}\mu_X(\rho^{(0)}_{GG}-\rho^{(0)}_{XX})(\omega-\omega_{X'}+i\gamma)E(\omega), \tag{A16}$$

where the term $\propto(\rho^{(0)}_{GG}-\rho^{(0)}_{X'X'})$ has been neglected, and

$$\mathcal{D}_0=(\omega-\omega_X+i\gamma)(\omega-\omega_{X'}+i\gamma)-4\Omega_R^2. \tag{A17}$$

Thus, one finds two resonances at

$$\omega_\pm=\omega_X+\tfrac{1}{2}\{\omega_{X'X}\pm[\omega^2_{X'X}+4(\gamma^2+4\Omega_R^2)]^{1/2}\}. \tag{A18}$$

Equation (A18) applies to any dc field strength. The lower-energy exciton level is redshifted while the higher-energy exciton level is blueshifted, both shifting by the same energy. Two limiting cases are of interest. (i) $\Omega_R\ll\omega_{X'X}$ (weak THz field): the resonances reduce to $\omega_-=\omega_X-(\gamma^2+4\Omega_R^2)/\omega_{X'X}$ and $\omega_+=\omega_{X'}+(\gamma^2+4\Omega_R^2)/\omega_{X'X}$. This is the second-order effect. (ii) $\Omega_R\gg\omega_{X'X}$ (extremely strong THz field): the resonances become $\omega_-=\omega_X-(\gamma^2+4\Omega_R^2)^{1/2}$ and $\omega_+=\omega_{X'}+(\gamma^2+4\Omega_R^2)^{1/2}$. This is the first-order effect. In the following we deduce result for low-Ω THz fields. For simplicity we neglect polarization dephasing.

(i) SOSE: when the NIR frequency ω varies about ω_X, Eq. (A16) can be transformed as

$$\hbar\frac{\partial}{\partial t}[\rho^{(1)}_{XG}(\omega)e^{i\omega_- t}]=i\mu_X(\rho^{(0)}_{GG}-\rho^{(0)}_{XX})\frac{\omega-\omega_{X'}}{\omega-\omega_+}E(\omega)e^{i\omega_- t}. \tag{A19}$$

As $\Omega_R\propto E_T$, we replace the dc Stark shift $4\Omega_R^2/\omega_{X'X}$ with $(4\Omega_R^2/\omega_{X'X})\cos^2\Omega t'$. The frequency shift in the resonance ω_- at time instant t is the averaged value of $(4\Omega_R^2/\omega_{X'X})\cos^2\Omega t'$ over the period from $t'=0$ to $t'=t$,[12] i.e., $(2\Omega_R^2/\omega_{X'X})[1+(\sin 2\Omega t/2\Omega t)]$. The t'-dependent shift in ω_+ is averaged over a THz-field period T. Substituting the two averages for the shifts in $\omega_\pm$ and upgrading $\rho^{(1)}_{XG}(\omega)$ to $\rho_{XG}(t)$, Eq. (A19) becomes

$$\begin{aligned}\hbar\frac{\partial}{\partial t}&[\rho_{XG}(t)e^{i[\omega_X-(2\Omega_R^2/\omega_{X'X})]t}]\\&=i\mu_X(\rho^{(0)}_{GG}-\rho^{(0)}_{XX})\frac{\omega-\omega_{X'}}{\omega-\omega_+}E(\omega)\\&\quad\times e^{i[\omega_X-(2\Omega_R^2/\omega_{X'X})]t}e^{-i(\Omega_R^2/\omega_{X'X}\Omega)\sin 2\Omega t},\end{aligned} \tag{A20}$$

where $\omega_+=\omega_{X'}+(2\Omega_R^2/\omega_{X'X})$.

When $E_T\to 0$, Eqs. (A6) and (A7) show that only the A_0 component is finite, making ω_X the resonance of $\rho_{XG}(t)$. In the presence of a weak THz field, then even A's [odd B's] satisfying Eqs. (A6) and (A7) determine the

solution of $\rho_{XG}(t)$ $[\rho_{X'G}(t)]$ for ω near ω_X. Thus, $\rho_{XG}(t)=e^{-i\omega t}\Sigma_k A_k e^{-ik\Omega t}$. Multiplying on both sides by $\hbar e^{i[\omega_X-(2\Omega_R^2/\omega_{X'X})]t}$ and differentiating with respect to t, we find

$$\hbar\frac{\partial}{\partial t}[\rho_{XG}(t)e^{i[\omega_X-(2\Omega_R^2/\omega_{X'X})]t}]$$
$$=-i\hbar e^{i[\omega_X-(2\Omega_R^2/\omega_{X'X})]t}$$
$$\times e^{-i\omega t}\sum_k\left(\omega-\omega_X+\frac{2\Omega_R^2}{\omega_{X'X}}+k\Omega\right)A_k e^{-ik\Omega t}. \tag{A21}$$

Now equating the right-hand side terms of Eqs. (A20) and (A21) and using series orthogonality, we obtain the expansion coefficients A_k ($k=0,\pm2,\pm4,\pm6,\ldots$) and then $\rho_{XG}(t)$. It follows that the first-order susceptibility can be given by

$$\chi_X(\omega)=-\frac{1}{V}|\mu_X|^2\frac{1}{\hbar}(\rho_{GG}^{(0)}-\rho_{XX}^{(0)})\frac{\omega-\omega_{X'}}{\omega-\omega_+}$$
$$\times\sum_{n=-\infty}^{+\infty}\frac{1}{\omega-\omega_X+\dfrac{2\Omega_R^2}{\omega_{X'X}}+2n\Omega+i\gamma'}J_n\left(\frac{\Omega_R^2}{\Omega\omega_{X'X}}\right), \tag{A22}$$

where $J_n(x)$ is the Bessel function of the first kind and $i\gamma'$ accounts for the line broadening. Equation (A22) shows that a series of resonances occur near ω_X in the X excitonic absorption spectrum; the main absorption is redshifted to $\omega_X-(2\Omega_R^2/\omega_{X'X})$ (by half the dc Stark shift) while the sidebands are separated by 2Ω and fall off as $|J_n(\Omega_R^2/\Omega\omega_{X'X})|$. For the X' excitonic absorption near $\omega_{X'}$, one finds similar resonances but the main absorption is blueshifted to $\omega_{X'}+(2\Omega_R^2/\omega_{X'X})$.

The X absorption of course occurs near $\omega_{X'}$ as well (corresponding to ω_+ in the dc case). One then needs to transform Eq. (A16) into the expression for $\hbar\frac{\partial}{\partial t}[\rho_{XG}(t)e^{i\omega_+ t}]$. As odd A's are strongly coupled with even B's [including B_0, $B_0\propto(\omega-\omega_{X'}+i\gamma)^{-1}$] via Eqs. (A8) and (A9), they determine the solution of $\rho_{XG}(t)$ for $\omega\sim\omega_{X'}$: $\rho_{XG}(t)=e^{-i\omega t}\Sigma_l A_l e^{-il\Omega t}$. Repeating the process as before, one finds that resonances occur at $\omega=\omega_{X'}+(2\Omega_R^2/\omega_{X'X})-l\Omega$ ($l=\pm1,\pm3,\pm5,\ldots$). The X absorption at these resonances is located at $l\Omega$ from the blueshifted X' exciton peak and has magnitude $\propto|I_l(\Omega_R^2/\Omega\omega_{X'X})|$, where $I_l(x)=\frac{1}{\pi}\int_0^\pi\cos(l\theta+x\sin2\theta)d\theta$. These resonances correspond to energy levels associated with the X exciton but are formed around $\omega_{X'}$, and they and the resonances given by Eq. (A22) together correspond to the components into which the X exciton energy level breaks up due to the THz field. Similarly there are resonances around ω_X for the X' absorption.

(ii) FOSE: replacing the dc Stark shift by $2\Omega_R\cos\Omega t'$. Note however that the average of ω_+ over the THz-wave period T reduces to $\omega_{X'}$, causing the factor $(\omega-\omega_{X'})/(\omega-\omega_+)$ to be removed from Eq. (A16). Proceeding as in case (i) but expanding $\rho_{XG}(t)$ as Eq. (A3), one finds that resonances occur at $\omega=\omega_X-n\Omega$ ($n=0,\pm1,\pm2,\pm3,\ldots$); the main X absorption is unshifted while the sidebands are separated by Ω instead of 2Ω with magnitude $\propto|J_n(2\Omega_R/\Omega)|$. Similar result can be obtained for the X' absorption.

*j.zhang2@bath.ac.uk

[1] D. A. B. Miller, D. S. Chemla, T. C. Damen, A. C. Gossard, W. Wiegmann, T. H. Wood, and C. A. Burrus, Phys. Rev. Lett. **53**, 2173 (1984).
[2] C. Phillips, M. Y. Su, M. S. Sherwin, J. Ko, and L. Coldren, Appl. Phys. Lett. **75**, 2728 (1999).
[3] B. Ferguson and X.-C. Zhang, Nature Mater. **1**, 26 (2002).
[4] M. Y. Su, S. G. Carter, M. S. Sherwin, A. Huntington, and L. A. Coldren, Phys. Rev. B **67**, 125307 (2003).
[5] S. G. Carter, V. Ciulin, M. S. Sherwin, M. Hanson, A. Huntington, L. A. Coldren, and A. C. Gossard, Appl. Phys. Lett. **84**, 840 (2004).
[6] S. G. Carter, V. Ciulin, M. Hanson, A. S. Huntington, C. S. Wang, A. C. Gossard, L. A. Coldren, and M. S. Sherwin, Phys. Rev. B **72**, 155309 (2005).
[7] B. S. Williams, B. Xu, Q. Hu, and M. R. Melloch, Appl. Phys. Lett. **75**, 2927 (1999).
[8] P. G. Huggard, C. J. Shaw, S. R. Andrews, J. A. Cluff, and R. Grey, Phys. Rev. Lett. **84**, 1023 (2000).
[9] M. Bedoya and A. S. Camacho, Phys. Rev. B **72**, 155318 (2005).
[10] P. Kinsler, P. Harrison, and R. W. Kelsall, J. Appl. Phys. **85**, 23 (1999).
[11] Y. R. Shen, *The Principles of Nonlinear Optics* (Wiley, New York, 1984).
[12] S. H. Autler and C. H. Townes, Phys. Rev. **100**, 703 (1955).
[13] C. H. Townes and F. R. Merritt, Phys. Rev. **72**, 1266 (1947).
[14] J. Shah, *Ultrafast Spectroscopy of Semiconductors and Semiconductor Nanostructures*, Springer Series in Solid State Science Vol. 115 (Springer, Berlin, 1996).
[15] P. Y. Yu and M. Cardona, *Fundamentals of Semiconductors: Physics and Materials Properties* (Springer, Berlin, 2005).
[16] D. K. Kim and D. S. Citrin, Phys. Rev. B **76**, 125305 (2007).
[17] X. Chen, W. Batty, M. P. Earnshaw, D. W. E. Allsopp, and R. Grey, IEEE J. Quantum Electron. **34**, 1180 (1998).
[18] K. Johnsen and A.-P. Jauho, Phys. Rev. Lett. **83**, 1207 (1999).
[19] C. J. Dent, B. N. Murdin, and I. Galbraith, Phys. Rev. B **67**, 165312 (2003).
[20] A. Liu and C.-Z. Ning, J. Opt. Soc. Am. B **17**, 433 (2000).
[21] A. V. Maslov and D. S. Citrin, Phys. Rev. B **62**, 16686 (2000).
[22] A. V. Maslov and D. S. Citrin, Phys. Rev. B **64**, 155309 (2001).
[23] S.-L. Chuang, S. Schmitt-Rink, D. A. B. Miller, and D. S. Chemla, Phys. Rev. B **43**, 1500 (1991).
[24] G. D. Sanders and Y.-C. Chang, Phys. Rev. B **35**, 1300 (1987).
[25] H. Haug and S. W. Koch, *Quantum Theory of the Optical and Electronic Properties of Semiconductors* (World Scientific, Singapore, 1994).
[26] L. Allen and J. H. Eberly, *Optical Resonance and Two-Level*

Atoms (Wiley, New York, 1975).
[27] V. Ciulin, S. G. Carter, M. S. Sherwin, A. Huntington, and L. A. Coldren, Phys. Rev. B **70**, 115312 (2004).
[28] M. Y. Su, S. G. Carter, M. S. Sherwin, A. Huntington, and L. A. Coldren, Appl. Phys. Lett. **81**, 1564 (2002).
[29] I. Vurgaftman, J. R. Meyer, and L. R. Ram-Mohan, J. Appl. Phys. **89**, 5815 (2001).
[30] G. Bastard, *Wave Mechanics Applied to Semiconductor Heterostructures* (Halsted, New York, 1988).
[31] In fact, experimentally it is difficult to know the transmitted THz field strength as the exact size of the THz mode in the waveguide is difficult to measure (Ref. 4). For a THz beam with the power of 1 kW, for instance, the THz electric-field strength was estimated to be between 5 and 20 kV/cm (Ref. 4).
[32] J. Hader, J. V. Moloney, and S. W. Koch, IEEE J. Quantum Electron. **35**, 1878 (1999).
[33] X. Chen, M. P. Earnshaw, K. W. Goossen, W. Batty, D. W. E. Allsopp, and R. Grey, J. Appl. Phys. **85**, 7231 (1999).
[34] Here, replica(s) enclosed by quotation marks refers, in general, to any feature(s) around an excitonic energy position, following the use in Ref. 22 rather than the stricter definition used in this paper.
[35] F. Bassani and G. P. Parravicini, *Electronic States and Optical Transitions in Solids* (Pergamon Press, Oxford, 1975).
[36] J. H. Shirley, Phys. Rev. **138**, B979 (1965).